**Estimations of Global Shortwave Direct Aerosol Radiative Effects Above Opaque Water Clouds**

**Using a Combination of A-Train Satellite Sensors**

Meloë S. Kacenelenbogen [1]
Mark A. Vaughan [3]
Jens Redemann [4]
Stuart A. Young [5]
Zhaoyan Liu [3,5]
Yongxiang Hu [3]
Ali H. Omar [3]
Samuel LeBlanc [2],
Yohei Shinozuka [2],
John Livingston [2],
Qin Zhang [2],
Kathleen A. Powell [3]

[1]NASA Ames Research Center, Moffett Field, CA, USA
[2]Bay Area Environmental Research Institute, Sonoma, CA, USA
[3]NASA Langley Research Center, Hampton, VA, USA
[4]University of Oklahoma, 120 David L. Boren Blvd., Suite 5900, Norman, OK
[5]Science Systems and Applications, Inc., Hampton, Virginia, USA

*Correspondence to:* Meloë S. Kacenelenbogen (meloe.s.kacenelenbogen@nasa.gov)

24 **Abstract**

25 All-sky Direct Aerosol Radiative Effects (DARE) play a significant yet still uncertain role in climate.

26 This is partly due to poorly quantified radiative properties of Aerosol Above Clouds (AAC). We

27 compute global estimates of short-wave top-of-atmosphere DARE over Opaque Water Clouds (OWC),

28 $DARE_{OWC}$, using observation-based aerosol and cloud radiative properties from a combination of A-

29 Train satellite sensors and a radiative transfer model. There are three major differences between our

30 $DARE_{OWC}$ calculations and previous studies: (1) we use the Depolarization Ratio method (DR) on

31 CALIOP (Cloud Aerosol LIdar with Orthogonal Polarization) Level 1 measurements to compute the

32 AAC frequencies of occurrence and the AAC Aerosol Optical Depths (AOD), thus introducing fewer

33 uncertainties compared to using the CALIOP standard product; (2) we apply our calculations globally,

34 instead of focusing exclusively on regional AAC "hotspots" such as the southeast Atlantic; and (3)

35 instead of the traditional look-up table approach, we use a combination of satellite-based sensors to

36 obtain AAC intensive radiative properties. Our results agree with previous findings on the dominant

37 locations of AAC (South and North East Pacific, Tropical and South East Atlantic, northern Indian

38 Ocean and North West Pacific), the season of maximum occurrence and aerosol optical depths (a

39 majority in the 0.01-0.02 range and that can exceed 0.2 at 532 nm) over the globe. We find positive

40 averages of global seasonal $DARE_{OWC}$ between 0.13 and 0.26 W·m$^{-2}$ (i.e., a warming effect on climate).

41 Regional seasonal $DARE_{OWC}$ values range from -0.06 W ·m$^{-2}$ in the Indian Ocean, offshore from

42 western Australia (in March-April-May) to 2.87 W ·m$^{-2}$ in the South East Atlantic (in September-

43 October-November). High positive values are usually paired with high aerosol optical depths (>0.1) and

44   low single scattering albedos (<0.94), representative of, e.g., biomass burning aerosols. Because we use

45   different spatial domains, temporal periods, satellite sensors, detection methods, and/or associated

46   uncertainties, the $DARE_{OWC}$ estimates in this study are not directly comparable to previous peer-

47   reviewed results. Despite these differences, we emphasize that the $DARE_{OWC}$ estimates derived in this

48   study are generally higher than previously reported. The primary reasons for our higher estimates are (i)

49   the possible underestimate of the number of dust-dominated AAC cases in our study; (ii) our use of

50   Level 1 CALIOP products (instead of CALIOP Level 2 products in previous studies) for the detection

51   and quantification of AAC aerosol optical depths, which leads to larger estimates of AOD above OWC;

52   and (iii) our use of gridded 4ºx5º seasonal means of aerosol and cloud properties in our $DARE_{OWC}$

53   calculations instead of simultaneously derived aerosol and cloud properties from a combination of A-

54   Train satellite sensors. Each of these areas is explored in depth with detailed discussions that explain

55   both rationale for our specific approach and the subsequent ramifications for our DARE calculations.

**ACRONYMS**

| | |
|---|---|
| AAC | Aerosol-Above-Clouds |
| AAOD | Absorption Aerosol Optical Depth |
| AOD | Aerosol Optical Depth |
| $\tau^{DR}_{AAC}$ | Aerosol Optical Depth above clouds using the DR method |
| AeroCom | Aerosol Comparisons between Observations and Models |
| AERONET | AErosol RObotic NETwork |
| AMSR-E | Advanced Microwave Scanning Radiometer - Earth Observing System |
| ARCTAS | Arctic Research of the Composition of the Troposphere from Aircraft and Satellites |
| ASR | integrated Attenuated Scattering Ratio |
| BRDF | Bidirectional Reflectance Distribution Function |
| CAC | Clear Air above Cloud |
| CALIOP | Cloud Aerosol LIdar with Orthogonal Polarization |
| CALIPSO | Cloud-Aerosol Lidar and Infrared Pathfinder Satellite Observations |
| CERES | Clouds and the Earth's Radiant Energy System |
| CF | Cloud Fraction |
| CloudSat | NASA Earth observation satellite |
| COD | Cloud Optical Depth |

| | |
|---|---|
| CR | Color Ratio technique |
| $DARE_{all-sky}$ | Direct Aerosol Radiative Effect in all-sky conditions (cloudy and non-cloudy) |
| $DARE_{cloudy}$ | Direct Aerosol Radiative Effect in cloudy conditions |
| $DARE_{non-cloudy}$ | Direct Aerosol Radiative Effect in non-cloudy conditions (clear-skies) |
| $DARE_{OWC}$ | Direct Aerosol Radiative Effect above opaque water clouds |
| DISORT | DIScrete ORdinate Radiative Transfer solvers |
| DR | Depolarization Ratio technique |
| $\delta^{OWC}$ | layer-integrated volume depolarization ratio |
| $f_{AAC}$ | AAC frequency of occurrence |
| HSRL | High Spectral Resolution Lidar |
| IAB | Integrated Attenuated Backscatter |
| IBS | Integrated aerosol Backscatter |
| InWA | Indian ocean, offshore from West Australia |
| LUT | Look Up Table |
| LWP | Liquid Water Path |
| MBL | Marine Boundary Layer |
| MCD43GF | MODIS BRDF/Albedo/NBAR CMG Gap-Filled Products |
| MODIS | MODerate Imaging Spectroradiometer |
| $\eta^{OWC}$ | layer effective multiple scattering factor |

| | |
|---|---|
| NEAs | North East Asia |
| NEPa | North East Pacific ocean |
| NWPa | North West Pacific ocean |
| OMI | Ozone Monitoring Instrument |
| ORACLES | ObseRvations of Aerosols above CLouds and their intEractionS |
| OWC | Opaque Water Cloud |
| POLDER | Polarization and Directionality of Earth's Reflectances |
| PBL | Planetary Boundary Layer |
| $R_e$ | Cloud droplet effective radius |
| RT | Radiative Transfer scheme |
| $S_a$ | Aerosol extinction-to-backscatter (lidar) ratio |
| $S_c$ | Cloud extinction-to-backscatter (lidar) ratio |
| SCIAMACHY | Scanning Imaging Absorption Spectrometer for Atmospheric Cartography |
| SEAs | South East Asia |
| SEAt | South East Atlantic ocean |
| SEPa | South East Pacific ocean |
| SEVIRI | Spinning Enhanced Visible and InfraRed Imager |
| SNR | Signal-to-Noise Ratio |
| SS | Single Scattering |
| SSA | Single Scattering Albedo |

| SW | Short Wave |
| TAt | Tropical Atlantic ocean |
| TOA | Top Of Atmosphere |

## 1. Introduction

The Direct Aerosol Radiative Effect (DARE) is defined as the change in the upwelling radiative flux $(F^\uparrow)$ at the top of the atmosphere (TOA) due to aerosols. Measured values of DARE depend on the accuracy and the geometry of the observation(s), the concentrations of various atmospheric constituents (e.g., aerosols, clouds, and atmospheric gases) and their radiative properties, and the Earth's surface reflectance. All-sky DARE ($DARE_{all-sky}$) combines contributions from DARE under cloudy conditions ($DARE_{cloudy}$) and DARE under cloud-free conditions ($DARE_{non-cloudy}$):

$$DARE_{all-sky} = DARE_{cloudy} \times Cloud\ Fraction + DARE_{non-cloudy} \times (1 - Cloud\ Fraction) \qquad Eq.\ (1)$$

According to Yu et al., [2006], substantial progress has been made in the assessment of $DARE_{non-cloudy}$ using satellite and in situ data. Further evidence is provided in a companion to our study, Redemann et al. [2019], which use A-Train aerosol observations to constrain $DARE_{non-cloudy}$ and compares the results with AeroCom (Aerosol Comparisons between Observations and Models) results (see Appendix A for further details). However, traditional passive aerosol remote sensing techniques are limited only to clear-sky conditions and significant efforts are required to estimate $DARE_{cloudy}$. Moreover, simulations of $DARE_{cloudy}$ from various AeroCom models in Schulz et al. [2006] (see their figure 6) show large disparities. Our study focuses on Aerosol Above Cloud (AAC) scenes over the globe and subsequent estimates of $DARE_{cloudy}$ (i.e., the instantaneous short wave (SW) upwelling TOA reflected radiative fluxes due to clouds only minus SW upwelling TOA fluxes due to clouds with overlying aerosols). Let us note that, ideally, TOA $DARE_{cloudy}$ should include aerosols below, in-between and above clouds. Here we assume that TOA $DARE_{cloudy}$ is only caused by aerosols above clouds. Table 1 lists TOA SW

80     $DARE_{cloudy}$ results that use satellite observations in the literature, together with assumptions in their

81     calculations. Compared to the peer-reviewed studies of Table 1, our study marks a departure on three

82     accounts. First, most peer-reviewed $DARE_{cloudy}$ calculations focus primarily on the South East Atlantic

83     (SEAt e.g., [Chand et al., 2009, Wilcox et al., 2012, Peters et al., 2011, De Graaf et al., 2012, 2014,

84     Meyer et al., 2013, 2015, Peers et al., 2015, Feng and Christopher, 2015] in Table 1). Second, our

85     results use a combination of A-Train satellite sensors (i.e., MODIS-OMI-CALIOP), instead of the

86     Look-Up-Table (LUT) approach used in the other studies of Table 1, to obtain estimates of the intensive

87     aerosol radiative properties above clouds. Third, the peer-reviewed global $DARE_{cloudy}$ calculations in

88     Table 1 use standard products from the active satellite sensor Cloud Aerosol LIdar with Orthogonal

89     Polarization (CALIOP) for either AAC Aerosol Optical Depth (AOD) and/or aerosol and cloud vertical

90     distribution information in the atmosphere [Zhang et al., 2014, 2016, Matus et al., 2015, Oikawa et al.,

91     2013]. In our case, we estimate $DARE_{cloudy}$ globally by using an alternate method applied to CALIOP

92     Level 1 measurements [Hu et al., 2007b; Chand et al., 2008; Liu et al., 2015] to obtain AAC AOD and

93     the AAC frequency of occurrence. In the sections below, we explain why we have used such a method,

94     instead of other passive or active satellite sensor techniques.

95     **Table 1:** TOA SW $DARE_{cloudy}$ calculations that use satellite observations in the literature and specific

96     assumptions in the calculations. See also the theoretical study by Chang and Christopher et al. [2017]

97     (i.e. they impose fixed COD, Re, AOD, aerosol radiative properties, and aerosol / cloud vertical

98     distribution) and the study by Costantino and Bréon et al. [2013] (their method uses MODIS-derived

99     cloud microphysics that are not corrected for overlying aerosols). When not specified, the study uses the

00     standard CALIOP data product; otherwise, it uses the DR (Depolarization Ratio) or CR (Color Ratio)

01 technique on CALIOP measurements. MODIS[A] and MODIS[T] respectively denote the AQUA or

02 TERRA platform. SEAt: South East Atlantic. LUT: Look Up Table. See acronyms for satellite sensors

03 MODIS, CALIOP, CloudSat, POLDER, CERES and AMSR-E.

| Reference | Domain | Satellite sensor(s) used for DARE$_{cloudy}$ calculations | | | |
|---|---|---|---|---|---|
| | | Cloud properties (e.g. COD, albedo, fraction) | AOD | Aerosol radiative properties (e.g. SSA, g) | Vertical distribution of aerosol and cloud |
| Chand et al. [2009] | SEAt | MODIS[T] | CALIOP[CR] | Fixed value | Assumed constant |
| Wilcox [2012] | SEAt | MODIS[A], AMSR-E | CERES provides upwelling shortwave flux | | |
| Peters et al. [2011] | Atlantic | MODIS[A], AMSR-E | CERES provides upwelling shortwave flux | | |
| De Graaf et al. [2012, 2014] | SEAt | Direct determination of DARE$_{cloudy}$ by building LUT of cloud and aerosol-free reflectances | | | |
| Meyer et al. [2013] | SEAt | MODIS[A] | CALIOP | LUT approach | CALIOP |
| Zhang et al. [2014, 2016] | Globe | MODIS[A], CALIOP (uses probability density function of CALIOP above-cloud AOD and underlying MODIS COD) | | LUT approach | CALIOP |
| Meyer et al. [2015] | SEAt | MODIS[A] (simultaneous retrieval of above-cloud AOD, COD and R$_e$) | | LUT approach | Assumed constant |
| Peers et al. [2015] | SEAt | POLDER (simultaneous retrieval of above-cloud aerosol OD, size and single scattering albedo, cloud optical depth and cloud top height) | | | |
| Feng and Christopher [2015] | SEAt | MODIS[A], CERES | CERES provides upwelling shortwave flux | | |

| Reference | Domain | Satellite sensor(s) used for DARE$_{cloudy}$ calculations | | | |
| --- | --- | --- | --- | --- | --- |
| | | Cloud properties (e.g. COD, albedo, fraction) | AOD | Aerosol radiative properties (e.g. SSA, g) | Vertical distribution of aerosol and cloud |
| Matus et al. [2015] | Globe | CloudSat, MODIS[A], CALIOP | CALIOP | LUT approach | CloudSat, CALIOP |
| Oikawa et al. [2013] | Globe | CALIOP, MODIS[A] | CALIOP | LUT approach | CALIOP |
| This study | Globe | MODIS[A] | CALIOP[DR] | MODIS[A], OMI, CALIOP | Assumed constant |

04

Table 2 lists some passive (i.e., Spinning Enhanced Visible and InfraRed Imager, SEVIRI, Moderate Resolution Imaging Spectroradiometer, MODIS, Polarization and Directionality of Earth's Reflectances, POLDER, Ozone Monitoring Instrument, OMI or the Scanning Imaging Absorption Spectrometer for Atmospheric Chartography, SCIAMACHY) and active (i.e., CALIOP and CloudSat) satellite sensors that were used to detect and quantify the AAC AODs. Among the peer-reviewed studies of Table 2, those few that present DARE$_{cloudy}$ results (see Table 1) are denoted by a "+" sign in the first column.

**Table 2:** Studies that observe AAC using passive and active satellite sensors (i.e., from left to right, SEVIRI, POLDER, CloudSat, OMI, MODIS, SCIAMACHY, CALIOP; see acronyms). When using CALIOP, the authors either use the standard Level 2 products (Std), the Depolarization method (DR) [Hu et al., 2007b] or the color ratio method (CR) [Chand et al., 2008]. SEAt stands for SE Atlantic,

16 SEAs for SE Asia, NEAs for NE Asia and TAt for Tropical Atlantic. The "+" sign in the first column

17 denotes the presence of DARE$_{cloudy}$ calculations.

| | Reference | Domain | Satellite sensor(s) used for aerosol-above-cloud detection | | | | | | |
|---|---|---|---|---|---|---|---|---|---|
| | | | SEVIRI | POLDER | CloudS | OMI | MODIS | SCIAMA | CALIOP |
| 1 | Chang and Christopher [2016, 2017[+]] | SEAt | ▓ | | | | ▓ | | |
| 2 | Waquet et al. [2013a] | Globe | | ▓ | | | | | |
| 3 | Waquet et al. [2009, 2013b] | SEAt, TAt | | ▓ | | | | | |
| 4 | Peers et al. [2015][+] | SEAt | | ▓ | | | | | |
| 5 | Jethva et al [2013, 2014] | SEAt, TAt | | | | | ▓ | | |
| 6 | Torres et al. [2012] | SEAt | | | | ▓ | | | |
| 7 | Peters et al. [2011][+] | Atlantic | | | | ▓ | | | |
| 8 | De Graaf et al. [2012, 2014][+] | SEAt | | | | | | ▓ | |
| 9 | Meyer et al. [2015][+] | SEAt | | | | | ▓ | | |
| 10 | Feng and Christopher [2015][+] | SEAt | | | | | ▓ | | |
| 11 | Sayer et al. [2016] | SEAt, SEAs | | | | | ▓ | | |
| 12 | Matus et al. [2015][+] | Globe | | | ▓ | | | | Std |
| 13 | Alfaro-Contreras et al. [2016] | Globe | | | | ▓ | ▓ | | Std |
| 14 | Alfaro-Contreras et al. [2014] | SEAt, SEAs | | | | ▓ | ▓ | | Std |
| 15 | Devasthale and Thomas [2011] | Globe | | | | | | | Std |
| 16 | Yu et al. [2012] | SEAt, TAt | | | | ▓ | ▓ | | Std |
| 17 | Wilcox [2012][+] | SEAt | | | | ▓ | | | Std |
| 18 | Meyer et al. [2013][+] | SEAt | | | | | | | Std |
| 19 | Zhang et al. [2014, 2016][+] | Globe | | | | | | | Std |
| 20 | Oikawa et al. [2013][+] | Globe | | | | | ▓ | | Std |
| 21 | Chung et al. [2016] | Globe | | | | | | | Std |
| 22 | Chand et al. [2008] | SEAt | | | | | | | CR, DR |

| | Reference | Domain | Satellite sensor(s) used for aerosol-above-cloud detection | | | | | | |
|---|---|---|---|---|---|---|---|---|---|
| | | | SEVIRI | POLDER | CloudS | OMI | MODIS | SCIAMA | CALIOP |
| 23 | Chand et al. [2009][+] | SEAt | | | | | | | CR |
| 24 | Deaconu et al. [2017] | Globe | | | | | | | Std, DR |
| 25 | Liu et al. [2015] | SEAt, TAt | | | | | | | DR |
| 26 | This study[+] | Globe | | | | | | | DR |

19    The brightening of clear patches near clouds [Wen et al., 2007] (i.e., "3-D cloud radiative effect" or

20    "cloud adjacency effect") can introduce biases into the current passive satellite AAC retrieval

21    techniques (i.e., lines 1-11 of Table 2). To minimize these biases, this study relies primarily on CALIOP

22    observations [Winker et al., 2009]. CALIOP is a three-channel elastic backscatter lidar with a narrow

23    field of view and a narrow source of illuminating radiation, which limits cloud adjacency effects and the

24    subsequent cloud contamination of aerosol data products [Zhang et al., 2005; Wen et al., 2007; Várnai

25    and Marshak, 2009]. CALIOP measures high-resolution (1/3 km in the horizontal and 30m in the

26    vertical in low and middle troposphere) profiles of the attenuated backscatter from aerosols and clouds

27    at visible (532 nm) and near-infrared (1064 nm) wavelengths along with polarized backscatter in the

28    visible channel [Hunt et al., 2009]. These data are distributed as part of the Level 1 CALIOP products.

29    The Level 2 products are derived from the Level 1 products using a succession of sophisticated retrieval

30    algorithms [Winker et al., 2009]. The Level 2 processing is composed of a feature detection scheme

31    [Vaughan et al., 2009], a module that classifies features according to layer type (i.e., cloud versus

32    aerosol) [Liu et al., 2010] and subtype (i.e., aerosol species) [Omar et al., 2009], and, finally, an

33    extinction retrieval algorithm [Young and Vaughan, 2009] that retrieves profiles of aerosol backscatter

34    and extinction coefficients and the total column AOD based on modeled values of the extinction-to-

35 backscatter ratio (also called lidar ratio and represented by the symbol $S_a$) inferred for each detected

36 aerosol layer subtype.

37 A few studies use standard CALIOP Level 2 Aerosol and Cloud Layer products to determine AAC

38 occurrence over the globe (see line 12-21 in Table 2). However, a study by Kacenelenbogen et al.

39 [2014] demonstrates that the standard version 3 CALIOP aerosol products substantially underreport the

40 occurrence frequency of AAC when aerosol optical depths are less than ~0.02, mostly because these

41 tenuous aerosol layers have attenuated backscatter coefficients less than the CALIOP detection

42 threshold. CALIOP's standard extinction (and optical depth) data products are only retrieved between

43 the tops and bases of detected features, and these boundaries may significantly underestimate the full

44 vertical extent of the layer (Kim et al., 2017; Thorsen et al., 2017; Toth et al., 2018). Furthermore, the

45 Kacenelenbogen et al. [2014] study found essentially no correlation between AAC AOD results

46 reported by the CALIOP and collocated NASA Langley airborne High Spectral Resolution Lidar

47 (HSRL). A subsequent study by Liu et al. [2015] shows that the CALIOP Level 2 standard aerosol data

48 products underestimate dust AAC AOD by ~26% over the Tropical Atlantic and smoke AAC AOD by

49 ~39% over the SE Atlantic.

50 For these reasons, a few studies in Table 2 (see line 22-26) use alternate methods on Level 1 CALIOP

51 products, such as the Color Ratio (CR) [Chand et al., 2008] or the Depolarization Ratio (DR) [Hu et al.,

52 2007b; Liu et al., 2015] methods, instead of using the AOD reported in the CALIOP standard Level 2

53 products.

54    In this study, we use the DR method and a combination of CALIOP Level 1 and Level 2 data products

55    to compute global estimates of the AAC frequency of occurrence (i.e., $f_{AAC}$) and the AAC AOD (i.e.,

56    $\tau^{DR}_{AAC}$) (section 2.1). We then use CALIOP results of $f_{AAC}$, $\tau^{DR}_{AAC}$ and other A-Train satellite products

57    to compute global $DARE_{cloudy}$ (section 2.2). Section 3 describes the geographical and seasonal

58    distribution of global $f_{AAC}$ (section 3.1), $\tau^{DR}_{AAC}$ (section 3.2) and $DARE_{cloudy}$ results (section 3.3).

59    Section 4 revisits some of the limitations in the method and proposes ways to improve on these

60    $DARE_{cloudy}$ calculations.

61    **2.  Method**

62        **2.1.    AAC optical depth**

63    Because the CALIOP backscatter signal is totally attenuated below the lowest "feature" detected within

64    any profile [Vaughan et al., 2009], this lowest feature is defined as being opaque.  Approximately 69%

65    of the time, the opaque feature detected in a profile is the Earth's surface [Guzman et al., 2017].  In the

66    remainder of the cases, the opaque feature is either a water cloud, an ice cloud, or, very rarely, an

67    aerosol layer.

68    The DR method, which is also known as the "constrained opaque water cloud method" [Liu et al,

69    2015], relies on Opaque Water Clouds (OWCs) as reflectivity targets. The OWCs in this study are

70    selected using the five criteria listed in Table B2 of the appendix. Most importantly, (1) only one cloud

71    can be detected within a 5 km (15 shot) along-track average (which means, for example, that marine

72    stratus below thin cirrus are excluded), and (2) this one cloud must be opaque (i.e., lowest feature

73    detected in a column, and not subsequently classified as a surface return). Furthermore, all OWCs must

74  be (3) spatially uniform (i.e., detected at single-shot resolution within every laser pulse included in the 5

75  km averaging interval), (4) assigned a high confidence score by the CALIOP cloud-aerosol

76  discrimination (CAD) algorithm and (5) identified as a high confidence water cloud by the CALIOP

77  cloud phase identification algorithm. When there is aerosol above OWCs, the lidar backscatter signal

78  received from the underlying water cloud is reduced in direct proportion to the two-way transmittance

79  of the aerosol layer above. However, because the DR retrieval technique requires backscatter

80  measurements from opaque water clouds [Hu et al., 2007b], it cannot be used to retrieve AOD from

81  aerosols lying above the low, transparent water clouds that are frequently observed over remote oceans,

82  especially in the southern hemisphere (e.g., Leahy et al. [2012]; Mace and Protat [2018]; O et al.

83  [2018]).

84  Based on Hu et al. [2007a, 2007b], Eq. (2) describes how we compute $\tau^{DR}_{AAC}$ using the DR method

85  above OWCs.

86  $\tau^{DR}_{AAC} = -0.5 \times \ln[IAB^{OWC}_{SS,AAC} / IAB^{OWC}_{SS,CAC}]$                                                Eq. (2)

87  Here $IAB^{OWC}_{SS,AAC}$ is the single scattering value (subscript SS) of the layer-integrated attenuated

88  backscatter (IAB) for an OWC underlying one or more aerosol layer(s) above the cloud. $IAB^{OWC}_{SS,CAC}$

89  is the single scattering value of the IAB for an OWC underlying Clear air Above Cloud (CAC). By

90  CAC, we mean that there are no aerosols detected above the OWC. In this study, we consider $\tau^{DR}_{AAC}$

91  valid when positive. According to Eq. (2), this means that $IAB^{OWC}_{SS,AAC}$ needs to always be smaller in

92  magnitude than $IAB^{OWC}_{SS,CAC}$ and $\tau^{DR}_{AAC}$ equals zero when $IAB^{OWC}_{SS,AAC}$ equals $IAB^{OWC}_{SS,CAC}$.

93   Section B of the appendix provides additional information about the application of Eq. (2) and the

94   various steps needed to derive $\tau^{DR}_{AAC}$. We list the selection criteria used to identify the OWC dataset in

95   this study and describe the corrections required to obtain single-scattering estimates of IAB from

96   measurements that contain substantial contributions from multiple scattering (B1). We also describe the

97   technique used for distinguishing between CAC and AAC conditions (B2), and illustrate our derivation

98   of an empirical parameterization of $IAB^{OWC}_{SS,CAC}$ as a global function of latitude and longitude (B3).

99   As reported in Table 2, the CALIOP DR method was used to study the African dust transport pathway

00   over the Tropical Atlantic [Liu et al., 2015] and the African smoke transport pathway over the South

01   East Atlantic [Liu et al., 2015; Chand et al., 2008, 2009]. More recently, the CALIOP DR method was

02   also used by Deaconu et al. [2017] to assess POLDER AAC AOD values [Waquet et al., 2009, 2013b

03   and Peers et al., 2015] over the globe. In this study, we extend the previous regional studies of [Liu et

04   al., 2015 and Chand et al., 2008, 2009] to derive global CALIOP-based AAC AOD estimates. Let us

05   note that, in our study, the accuracy of $\tau^{DR}_{AAC}$ depends on measurements of targets of very high signal-

06   to-noise ratio (SNR) such as OWCs in clear skies and OWCs underlying aerosol layers.

07   ## 2.2.    AAC Direct Aerosol Radiative Effects

08   Having first retrieved global values of $\tau^{DR}_{AAC}$ from the CALIOP measurements, we then compute

09   global estimates of $DARE_{cloudy}$ using DISORT (DIScrete ORdinate Radiative Transfer; Stamnes et al.,

10   1988, Buras et al., 2011), a six-stream plane-parallel radiative transfer model with molecular absorption

11   characterized by a correlated-k scheme [Fu and Liou, 1992] that is embedded within the LibRadtran

12   Radiative Transfer (RT) package [Emde et al., 2016]. Hereafter, our seasonally and spatially gridded (4º

13 x 5º) averaged shortwave (SW) (250 nm to 5600 nm) global TOA $DARE_{cloudy}$ results will be called

14 $DARE_{OWC}$, as they pertain to a specific category of clouds (i.e., OWCs) defined according to the

15 CALIOP data selection criteria set forth in Table B2. We list the following input parameters to DISORT

16 in order to derive estimates of $DARE_{OWC}$:

17 (1) **Atmospheric profiles** of pressure, temperature, air density, ozone, water vapor, $CO_2$, and $NO_2$

18 use standard US atmosphere profiles [Anderson et al., 1986].

19 (2) **Aerosol intensive radiative properties** (i.e. properties that depend solely on aerosol species,

20 and are unrelated to the aerosol amount) are informed by seasonal maps (4º x 5º, daytime in 2007)

21 of combined MODIS-OMI-CALIOP (MOC) retrieved median spectral extinction coefficients,

22 single scattering albedos and asymmetry parameters at 30 different wavelengths. As an example,

23 Figure A1 in the appendix shows the seasonal maps of MOC SSA at 546.3 nm that were used in the

24 calculation of $DARE_{OWC}$. These MOC retrievals, described in section A of the appendix, are at the

25 basis of a companion study [Redemann et al., 2019]. Let us note that we only use the shape of the

26 MOC extinction coefficient spectra and not its actual magnitude; the MOC spectral extinction

27 coefficient spectra is normalized to the seasonal 2008-2012 average value of either $\tau^{DR}_{AAC}$ or $\tau^{DR}_{AAC}$

28 x $f_{AAC}$ within each grid cell. Our method assumes similar aerosol radiative properties above clouds

29 and in near-by clear-sky regions.

30 (3) **Aerosol extensive radiative properties** (i.e., properties that depend on the aerosol amount

31 present in the atmosphere) are informed by seasonal maps (4º x 5º, nighttime from 2008 to 2012) of

32 either CALIOP $\tau^{DR}_{AAC}$ (see Eq. 2) or CALIOP $\tau^{DR}_{AAC}$ x $f_{AAC}$. We chose to use nighttime CALIOP

33       $\tau^{DR}_{AAC}$ or $\tau^{DR}_{AAC}$ x $f_{AAC}$ results in the estimation of $DARE_{OWC}$ because, at nighttime, the CALIOP

34       signal-to-noise-ratio (SNR) is not affected by ambient solar background and leads to a more

35       accurate measurement of the aerosol signal (compared to daytime). By doing this, we implicitly

36       chose a better accuracy in the aerosol extensive radiative properties over a temporal overlap

37       between aerosol extensive (nighttime) and intensive (daytime) radiative properties.

38       (4) **Cloud albedos** are computed from cloud droplet effective radius ($R_e$) and Cloud Optical Depth

39       (COD) information inferred from MODIS averaged monthly 1º×1º grids (i.e. liquid water cloud

40       products of MYD08_M3: "Cloud Effective Radius Liquid Mean Mean" and "Cloud Optical

41       Thickness Liquid Mean Mean" [Platnick et al. 2015]) from 2008 to 2012 (see Equations 1-9 of Peng

42       et al. [2002]). These maps are then further gridded (to 4º×5º) and seasonally averaged to match the

43       format of the aerosol radiative properties. Appendix figure A2 shows the seasonal maps of MODIS

44       COD that were used in the calculation of $DARE_{OWC}$.

45       (5) **Aerosol and cloud layer heights** are assumed constant over the globe (respectively between 3-

46       4km and 2-3km in this study), similar to other studies in Table 1 (e.g., Meyer et al. [2015]).

47       (6) **Earth's surface albedo** uses global gap-filled Terra and Aqua combined MODIS BRDF/albedo

48       products. It uses the 16-day closest product (i.e., MCD43GF) to the middle of each season (i.e., Jan

49       15th for DJF, April 15th for MAM, July 15th for JJA and October 15th for SON). In the open ocean,

50       the Cox and Munk [1954] sea surface albedo parameterization is applied with a wind speed of 10

51       ms$^{-1}$.

52 Using these inputs, Daily $DARE_{OWC}$ results for each of the 4º × 5º grid cells are obtained by averaging

53 24 LibRadtran RT calculations, corresponding to 24 different sun positions at each hour of the day.

54 ### 3. Results

55 ### 3.1. AAC Occurrence Frequencies

56 To provide the necessary context for interpreting our TOA radiative transfer calculations, we first

57 establish the observational AAC occurrence frequencies from which we will subsequently compute

58 estimates of $DARE_{OWC}$. Figure 1 illustrates the annual gridded mean (5 years) global occurrence

59 frequencies of a) single layer clouds, b) opaque water clouds that are suitable for the DR method and c)

60 aerosol-above-clouds cases using the DR method. Figure 1d) shows the difference between the number

61 of AAC cases using the DR method (i.e., number of cases with $\tau^{DR}_{AAC} > 0$) and the number of AAC

62 cases using the standard Version 3 CALIOP product.

**Figure 1:** During nighttime, from 2008 to 2012 on a 4º×5º-grid: Occurrence frequencies of (a) uniform single layer clouds (C1-C3 of Table B2), (b) opaque water clouds suitable for the DR method (C1-C5 of Table B2; these clouds can be obstructed or unobstructed) and (c) AAC cases that show a positive $\tau^{DR}_{AAC}$ at 532 nm. (d) shows the difference between the number of AAC cases using the DR method (i.e., number of cases with $\tau^{DR}_{AAC} > 0$) and the number of AAC cases using the standard Version 3 CALIOP product (i.e., number of cases with $\tau^{STD}_{AAC} > 0$); CALIOP AAC cases using the standard algorithm are defined as 5 km-columns showing an uppermost layer classified as aerosols and a cloud

72   layer anywhere below that aerosol layer; the cloud itself does not have to satisfy any of the criteria of

73   Table B2. Grid cells are 4º x 5º latitude/ longitude. The percentages in (a)-(d) use the number of 5 km

74   CALIOP samples within each grid cell as a reference. White pixels show either no CALIOP

75   observations, no CALIOP OWC detection, a small number of CALIOP unobstructed OWCs or a small

76   number of positive $\tau^{DR}_{AAC}$ values. The title of each map shows the global maximum, median and mean

77   values.

79   Uniform single layer clouds (i.e. C1-C3 of Table B2) are detected in ~47% of all 5 km CALIOP

80   samples over the globe (see Figure 1(a)). In other words, at any one time, approximately half of the

81   globe is covered by uniform single layer clouds. As expected, the highest occurrence of those clouds is

82   in the high and low latitude bands and especially over the southern oceans. According to Figure 1(b),

83   OWCs suitable for the DR method (i.e. C1-C5 of Table B2) are mostly in the marine stratocumulus

84   regions and represent a mean of 7% of all 5 km CALIOP samples over the globe. This significant

85   reduction from half-the-globe coverage is explained by the five criteria used to select OWCs for the

86   application of the DR method (i.e., C1-C5 of Table B2). The highest occurrence of OWCs can be found

87   offshore from the west coasts of North and South America, southwest Africa and Australia. In

88   particular, OWC cover ranges from 60 to 75 % over the region of SE Atlantic in August [Klein and

89   Hartmann, 1993]. Also, the southeastern Pacific region off the Peruvian and Chilean coasts is the

90   location of the largest and most persistent stratocumulus deck in the world [Klein and Hartmann, 1993].

91   The percentage of AAC cases (i.e., AAC cases showing positive $\tau^{DR}_{AAC}$) at the basis of our study is

92    very small compared to the total number of 5 km CALIOP profiles per grid cell (i.e. mean of 5% on

93    Figure 1(c)). This is primarily due to a small number of low OWC used for the DR method over the

94    globe (when comparing Figure 1(a) and 1(b)).

95    Figure 1(d) illustrates the difference in occurrence frequencies of AAC cases using the DR method

96    compared to the standard Version 3 CALIOP product. Negative values, shown in blue, indicate the

97    fraction of cases for which the DR method fails to detect above-cloud aerosols that are reported in the

98    standard CALIOP product.  Similarly, positive values, shown in red, indicate the number of cases for

99    which above-cloud aerosols are detected by the DR method but not reported in the standard CALIOP

00    data product. Unlike the AAC cases detected using the DR method, the AAC cases obtained from the

01    CALIOP standard product do not impose any restrictions on the nature of the underlying clouds.

02    Instead, the CALIOP standard product reports aerosol detected above both opaque and transparent

03    clouds, irrespective of cloud thermodynamic phase. The blue regions in Fig. 1(d) show that, relative to

04    the CALIOP standard product, our implementation of the DR method could be failing to detect AAC

05    cases over most of land surfaces and over the Arabian Sea, the Tropical Atlantic, and the SE Atlantic

06    regions. The lack of AAC cases offshore from the southwest coast of Africa in the DR method dataset is

07    the result of our conservative data filtering strategy.  Because the IABs of aerosol-contaminated OWCs

08    can differ significantly from those measured in pristine, aerosol-free conditions, OWCs suspected of

09    being aerosol-contaminated (which are ubiquitous in this part of the world and very common over

10    continents) are specifically excluded from our DR method analyses (see appendix section B3 for more

11    details). However, some regions such as the NE and SE Pacific exhibit up to 40% more AAC cases

12    when using the DR method. The SE Pacific region, especially offshore from Chile, shows particularly

13 tenuous aerosols, with attenuated backscatter values that typically fall below the CALIOP detection

14 limit, thus hampering the detection of AAC using the standard CALIOP algorithm [Kacenelenbogen et

15 al., 2014].

16 In the rest of this study, the frequency of occurrence of AAC, $f_{AAC}$, is defined as:

17 $f_{AAC} = N_{AAC}/N_{OWC}$                                         Eq. (3)

18 where $N_{AAC}$ is the number of AAC cases (i.e., cases showing a positive $\tau^{DR}_{AAC}$ at 532nm) and $N_{OWC}$ is

19 the number of OWCs within each 4º×5º grid cell. Let us note that different studies use different

20 references when computing the frequency of occurrence of AAC. The definition in Eq. (3) is similar to

21 the one in Zhang et al. [2016] (see their Eq. (1)) and different from Devasthale and Thomas [2011],

22 where $f_{AAC}$ is defined as the ratio of AAC cases to the total number of CALIOP observations (similar to

23 what is shown on Fig. 1(c)).

24 Figure 2 illustrates the global seasonal $f_{AAC}$ (see Eq. 3) from 2008 to 2012. We find a median global

25 $f_{AAC}$ of 58% to 61% with regional values that can reach more than 80% in some regions such as the SE

26 Atlantic, especially during the JJA season. The AAC occurrence frequencies in Fig. 2 generally agree

27 with previous findings [Zhang et al., 2016; Devasthale and Thomas, 2011] on the location and season of

28 highest $f_{AAC}$.
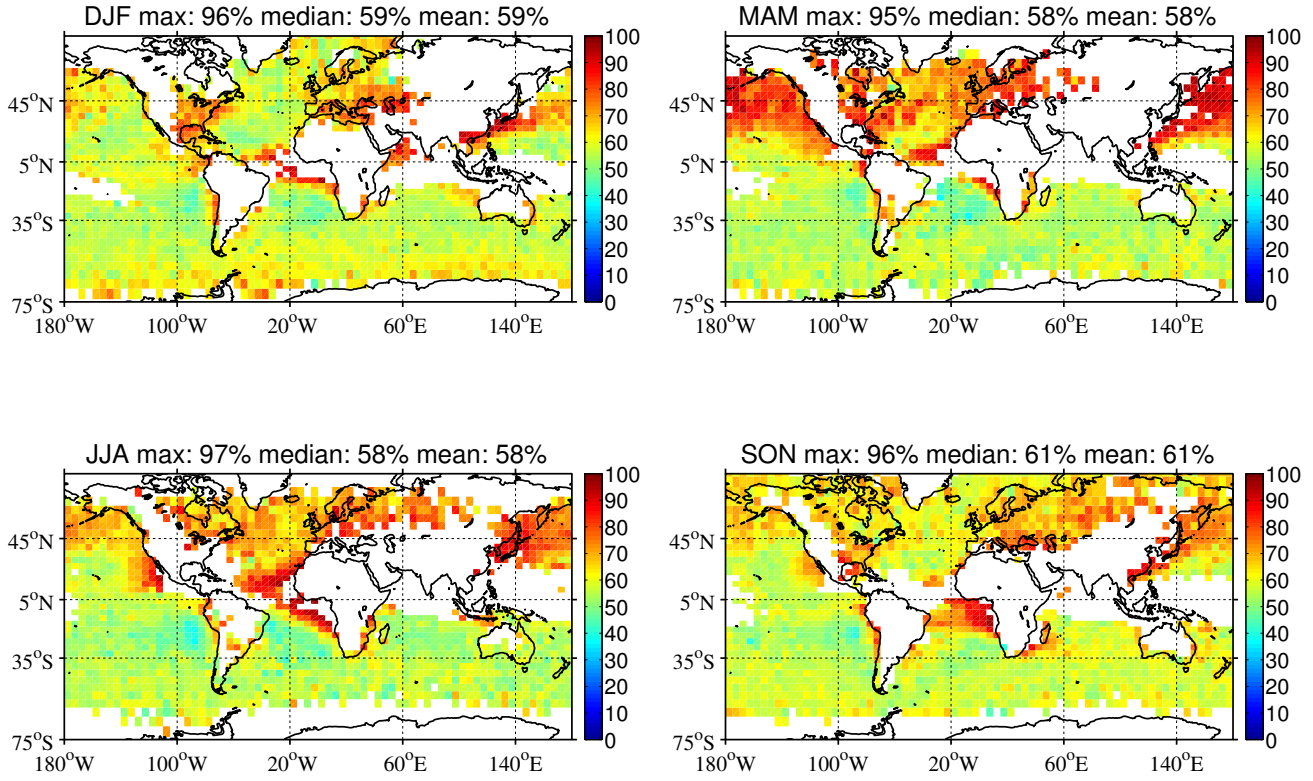
**Figure 2:** Global seasonal 4º×5º nighttime AAC occurrence frequency (noted $f_{AAC}$, see Eq. (3)) from 2008 to 2012. White pixels show either no CALIOP observations, a limited number of CALIOP unobstructed OWCs or a limited number of positive $\tau^{DR}_{AAC}$ values. White pixels are not considered in the global mean and median $f_{AAC}$ values in the title of each map. The title of each map shows the global maximum, median and mean values.

## 3.2.   AAC Optical Depths

39    Figure 3 introduces the global, nighttime and multi-year (2008-2012) AAC optical depths ($\tau^{DR}_{AAC}$, see

40    Eq. 2) dataset that was computed in this study.
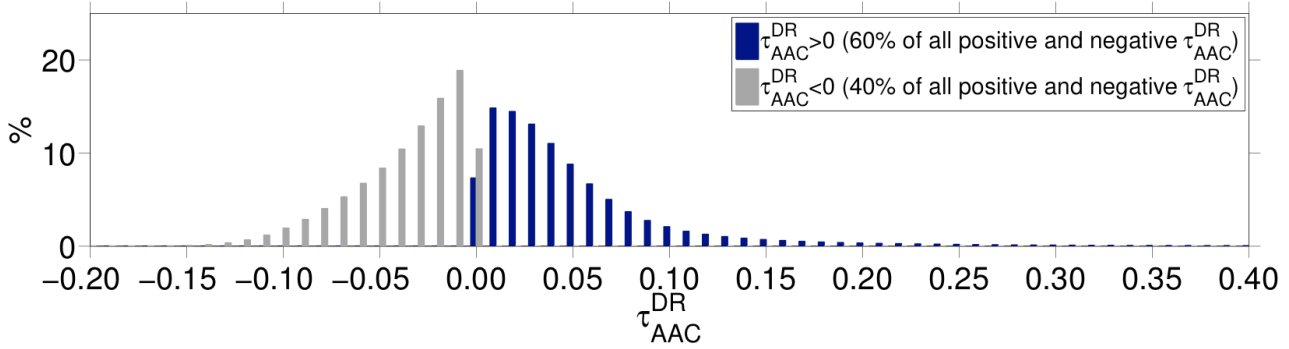
43    **Figure 3:** Global distribution of $\tau^{DR}_{AAC}$ at 532 nm. Positive (i.e., valid) $\tau^{DR}_{AAC}$ values are in dark blue

44    (N~3.4M) and negative $\tau^{DR}_{AAC}$ values in grey (N~2.2M). These are nighttime CALIOP measurements

45    from 2008-2012.

46    About 40% (i.e. 2.2M data points) of the initial dataset (i.e. N~5.6M) shows negative $\tau^{DR}_{AAC}$ values and

47    were flagged as invalid data (see Figure 3, in grey). When looking at all valid (i.e. positive) $\tau^{DR}_{AAC}$

48    values (blue), we show a majority of very small $\tau^{DR}_{AAC}$ values in the 0.01-0.02 AOD range. This agrees

49    with the findings of Devasthale and Thomas [2011]. Let us note that averaging all data points per 4°x5°

50    grid cell (instead of the native resolution shown on Fig. 3) increases the AOD bin of maximum AAC

51    occurrence globally from 0.01 (Fig. 3) to 0.03.

52    Table 3 shows four different ways of computing global seasonal and annual averages of aerosol optical

53    depth above clouds: we use either $\tau^{DR}_{AAC}$ or $\tau^{DR}_{AAC}$ x f$_{AAC}$ (see Case I-II or III-IV) and then either (i)

54 exclude all cases of $\tau^{DR}_{AAC} < 0$ from the average (i.e., as in Case I and Case III), or (ii) set all cases of

55 $\tau^{DR}_{AAC} < 0$ to zero, and include these samples in the averages (i.e., as in Case II and Case IV). Let us

56 note that using $\tau^{DR}_{AAC} \times f_{AAC}$ (instead of $\tau^{DR}_{AAC}$) acknowledges the fact that some OWCs present no

57 overlying aerosols. In this case, we assume that when the DR technique retrieves an invalid AAC

58 measurement, $f_{AAC} = 0$ and there are no aerosols above the cloud.

59 **Table 3:** Global seasonal and annual averages of $\tau^{DR}_{AAC}$ (Case I and II) or $\tau^{DR}_{AAC} \times f_{AAC}$ (Case III and

60 IV) when assuming either (i) $\tau^{DR}_{AAC} < 0$ cases are excluded from the averages (Case I and III) or

61 (ii) $\tau^{DR}_{AAC} < 0$ cases are set to zero and included in the averages (Case II and IV). Annual averages here

62 (last column) are the mean of the seasonal averages.

| Global mean aerosol optical depth | DJF | MAM | JJA | SON | Annual |
|---|---|---|---|---|---|
| Case I $\tau^{DR}_{AAC}$, invalid $\tau^{DR}_{AAC}$ excluded | 0.04 | 0.05 | 0.05 | 0.05 | 0.05 |
| Case II $\tau^{DR}_{AAC}$, invalid $\tau^{DR}_{AAC} = 0$ | 0.02 | 0.02 | 0.02 | 0.02 | 0.02 |
| Case III $\tau^{DR}_{AAC} \times f_{AAC}$, invalid $\tau^{DR}_{AAC}$ excluded | 0.03 | 0.03 | 0.04 | 0.03 | 0.03 |
| Case IV $\tau^{DR}_{AAC} \times f_{AAC}$, invalid $\tau^{DR}_{AAC} \times f_{AAC} = 0$ | 0.01 | 0.01 | 0.01 | 0.01 | 0.01 |

63 Figure 4 shows global seasonal nighttime median $\tau^{DR}_{AAC} \times f_{AAC}$ from 2008 to 2012 (i.e., as in Case III

64 of Table 3). The title of each seasonal map (respectively DJF, MAM, JJA, SON) in Figure 4 shows the

65 global maximum (respectively 0.11, 0.13, 0.22, 0.20), median (0.02 for all seasons) and mean (0.03 in

66 DJF, MAM and SON and 0.04 in JJA) $\tau^{DR}_{AAC} \times f_{AAC}$ values.
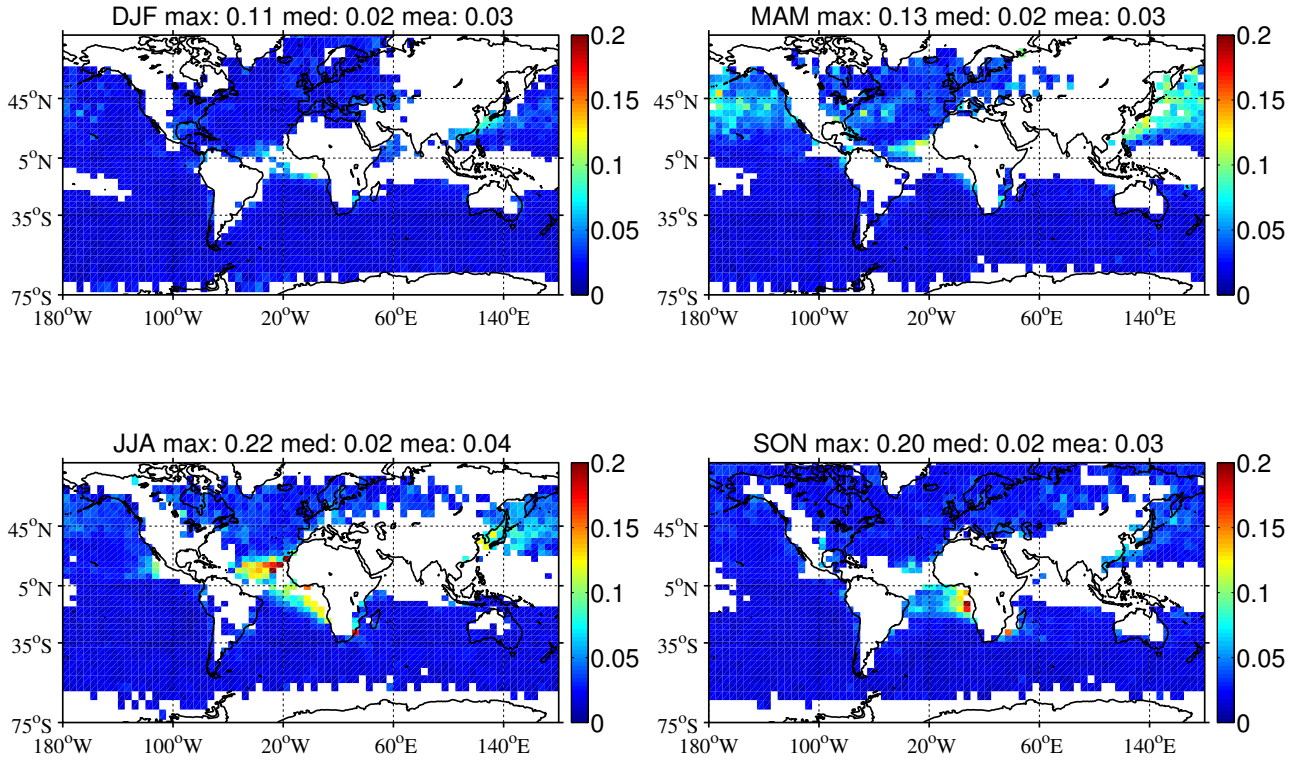
**Figure 4:** Global seasonal 4°x5° nighttime median $\tau^{DR}_{AAC}$ x $f_{AAC}$ from 2008 to 2012. Underlying clouds satisfy the criteria in Table B2. White pixels show either no CALIOP observations, a limited number of CALIOP unobstructed OWCs or a limited number of positive $\tau^{DR}_{AAC}$ values. White pixels are not included when calculating the global mean and median $\tau^{DR}_{AAC}$ values in the title of each map (i.e., as in Case III in Table 3). Note that if the white pixels were set equal to zero, the seasonal and annual global $\tau^{DR}_{AAC}$ values would correspond to Case IV in Table 3. The title of each map shows the global maximum, median and mean values.

77    We do not expect the $\tau^{DR}_{AAC}$ x $f_{AAC}$ values of Figure 4 to be similar to the results of [Zhang et al., 2014,

78    Devasthale and Thomas, 2011, Alfaro-Contreras et al., 2016 or Yu and Zhang, 2013] (see Table 2) as

79    these studies use standard CALIOP Level 2 aerosol and cloud layer products for AAC observations,

80    instead of using the DR method. On the other hand, the results of Figure 4 seem to be in qualitative

81    agreement with the global AAC AOD derived from spaceborne POLDER observations [Waquet et al.,

82    2013a]. Let us note that Waquet et al. [2013a] have to assume an underlying COD larger than 3 to

83    ensure the saturation of the polarized light scattered by the cloud layer. Although Deaconu et al. [2017]

84    make different assumptions in the application of the DR method on CALIOP measurements (e.g., they

85    impose a constant cloud lidar ratio for OWCs with clear air above), they find that POLDER and

86    CALIOP $\tau^{DR}_{AAC}$ are in good agreement over the SE Atlantic ($R^2 = 0.83$) and over the Tropical Atlantic

87    ($R^2 = 0.82$) from May to October 2008.

89    **3.3.      AAC Direct Aerosol Radiative Effects**

90      **3.3.1.  Global results of DARE$_{OWC}$**

91    Figure 5 shows the seasonal TOA SW DARE$_{OWC}$ estimates (W·m$^{-2}$) that use CALIOP $\tau^{DR}_{AAC}$ x $f_{AAC}$

92    (see Fig. 4) as input to a radiative transfer model, together with the other parameters described in

93    section 2.2. DARE$_{OWC}$ in Fig. 5 is set equal to zero (i.e., white pixels) if DARE$_{OWC}$ is invalid or

94    missing.

95

96
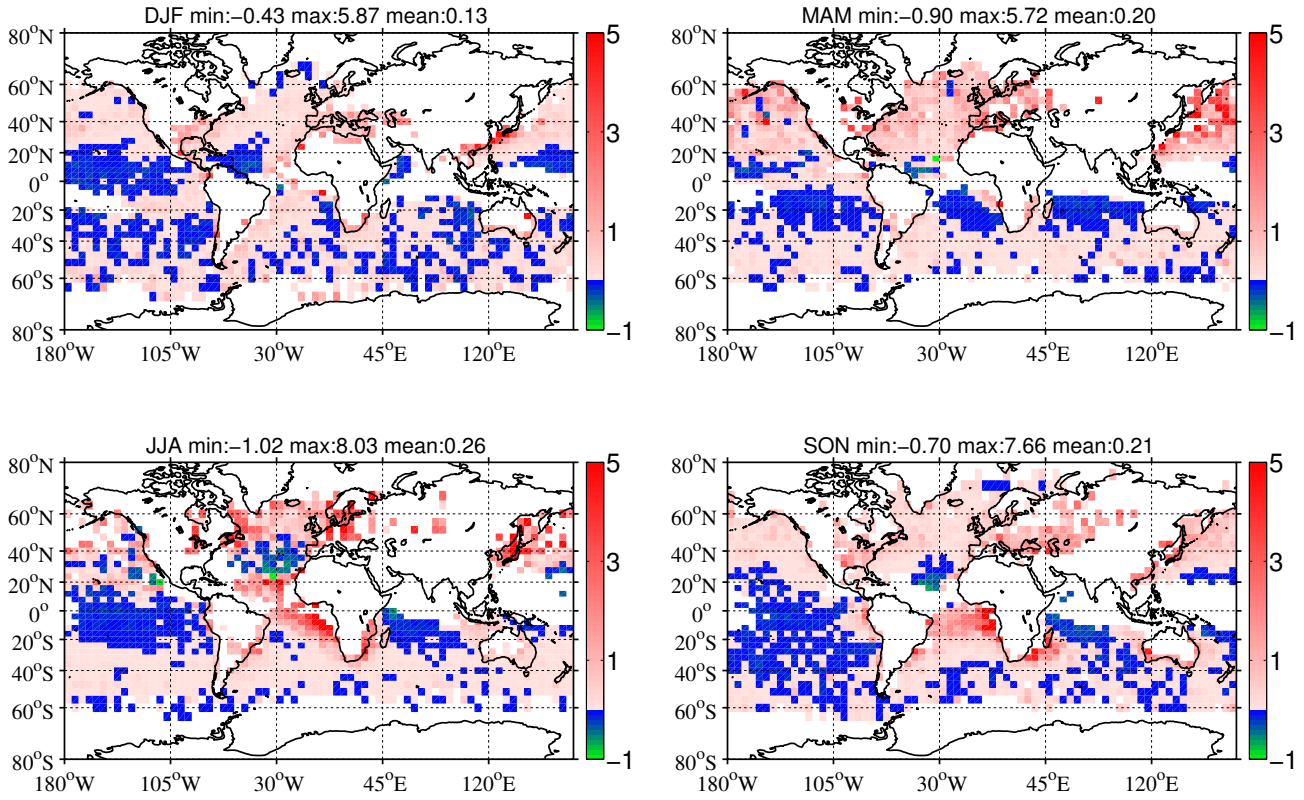
**Figure 5:** Global seasonal 4º×5º TOA SW DARE$_{OWC}$ estimates (W·m$^{-2}$, as described in section 2.2). A white pixel is counted as DARE$_{OWC}$=0 in the global mean DARE$_{OWC}$ values in the title of each map. White pixels show a limited number of CALIOP OWCs, positive $\tau^{DR}_{AAC}$ values or auxiliary MODIS-OMI-CALIOP combined satellite observations. The title of each map shows the global minimum, maximum, and mean values.

97

98

99

00

01

02

03

04  Similar to TOA $DARE_{cloudy}$ values from combined A-Train satellites in Oikawa et al. [2013] (see their

05  Fig. 10) and from General Circulation Models (GCMs) (e.g. SPRINTARS) in Shulz et al. [2006] (see

06  their Fig. 6 and 7), TOA $DARE_{OWC}$ values in Fig. 5 are mostly positive (i.e., a warming effect due to

07  less energy leaving the climate system) over the globe. We find, globally, 72% positive 4º×5º

08  $DARE_{OWC}$ values (i.e., N=4045) against 28% negative values (i.e., N=1581) when considering all four

09  seasons on Fig. 5. On the other hand, the highest negative TOA $DARE_{OWC}$ values on Fig. 5 (i.e.,

10  cooling effects shown in green pixels) are over the Tropical Atlantic (in MAM, JJA and SON), in the

11  Pacific Ocean offshore from Mexico (in JJA) and at the periphery of the Arabian Sea (in JJA).

12  There are multiple ways to compute the global seasonal and annual $DARE_{cloudy}$ averages (i.e.,

13  $DARE_{OWC}$ in our case), and it is not clear which method would bring us closer to the true $DARE_{cloudy}$

14  state of the planet. For this reason, we list several different methods in Table 4. We either use CALIOP

15  $\tau^{DR}_{AAC}$ or CALIOP $\tau^{DR}_{AAC}$ x $f_{AAC}$ (Case I-II or III-IV) and we either exclude invalid $DARE_{OWC}$ values

16  or set invalid $DARE_{OWC}$ = 0 (Case I-III or II-IV). For completeness and as an intermediate step towards

17  $DARE_{all-sky}$ (see Eq. 1), Case V and VI show the global seasonal averages of $DARE_{OWC}$ x Cloud Fraction

18  (CF), instead of $DARE_{OWC}$. The CF values use monthly MODIS AQUA MYD08_M3 products (variable

19  "Cloud Retrieva Fraction Liquid FMean"), which are seasonally averaged and 4º×5º-gridded.

21  **Table 4:** Global seasonal and annual averages of TOA SW $DARE_{OWC}$ estimates (W·m$^{-2}$, as described in

22  section 2.2). Annual averages (last column) are the mean of the seasonal averages (e.g., 0.53 for Case I

23  is the average of 0.34, 0.52, 0.71 and 0.56); CF stands for Cloud Fraction.

| Global averaged DARE$_{cloudy}$ (W $\times$ m$^{-2}$) | DJF | MAM | JJA | SON | Annual |
|---|---|---|---|---|---|
| Case I<br>DARE$_{OWC}$, $\tau^{DR}_{AAC}$, invalid DARE$_{OWC}$ excluded | 0.34 | 0.52 | 0.71 | 0.56 | 0.53 |
| Case II<br>DARE$_{OWC}$, $\tau^{DR}_{AAC}$, invalid DARE$_{OWC}$=0 | 0.19 | 0.26 | 0.35 | 0.29 | 0.27 |
| Case III<br>DARE$_{OWC}$, $\tau^{DR}_{AAC}$ x f$_{AAC}$, invalid DARE$_{OWC}$ excluded | 0.24 | 0.40 | 0.53 | 0.40 | 0.39 |
| Case IV<br>DARE$_{OWC}$, $\tau^{DR}_{AAC}$ x f$_{AAC}$, invalid DARE$_{OWC}$=0 | 0.13 | 0.20 | 0.26 | 0.21 | 0.20 |
| Case V<br>DARE$_{OWC}$ x CF, $\tau^{DR}_{AAC}$, invalid DARE$_{OWC}$ excluded | 0.11 | 0.16 | 0.25 | 0.19 | 0.18 |
| Case VI<br>DARE$_{OWC}$ x CF, $\tau^{DR}_{AAC}$ x f$_{AAC}$, invalid DARE$_{OWC}$=0 | 0.04 | 0.06 | 0.09 | 0.07 | 0.07 |

Global seasonal and annual DARE$_{OWC}$ averages (see titles in Fig. 5 and Table 4) in our study represent the surface area of each grid cell. Each valid DARE$_{OWC}$ value per pixel on each map of Fig. 5 is multiplied by the surface of the pixel. These values per grid cell are then summed up and divided by the sum of the surface of all valid grid cells.

Figure 5 corresponds to the setting of Case IV in Table 4. The reason why we have selected to showcase this setting is because it closely resembles the settings of the DARE$_{cloudy}$ calculations in Zhang et al. [2016]; i.e., it assumes DARE = 0 when CALIOP cannot detect an aerosol layer. Figure 5 shows positive global seasonal DARE$_{OWC}$ averages between 0.13 and 0.26 W·m$^{-2}$ (and an annual average of 0.20 W·m$^{-2}$ in Table 4) as well as the lowest DARE$_{OWC}$ values when compared to DARE$_{OWC}$

34     values from Case I through Case IV in Table 4. These values are nonetheless much larger than the

35     global annual ocean $DARE_{cloudy}$ values reported in Zhang et al. [2016] and Schulz et al. [2006] (e.g.,

36     annual average of 0.015 W $\times$ m$^{-2}$ reported over ocean in Zhang et al. [2016]). Moreover, Matus et al.

37     [2015] find (see their Table 2) a global TOA $DARE_{cloudy}$ value of 0.1 W·m$^{-2}$ over thick clouds (these

38     clouds are similar to our study), compensated by a global TOA $DARE_{cloudy}$ value of -2 W·m$^{-2}$ over thin

39     clouds.

40     Section 3.3.2 further analyzes $DARE_{OWC}$, together with $f_{AAC}$, $\tau^{DR}_{AAC}$, SSA, and COD results in a few

41     selected regions and compares these results to previous studies.

42     **3.3.2.  Regional results of $DARE_{OWC}$**

43     The $f_{AAC}$ results in Fig. 2 help us define six major AAC "hotspots" over the North East Pacific (NEPa),

44     South East Pacific (SEPa), Tropical Atlantic (TAt), South East Atlantic (SEAt), Indian ocean, offshore

45     from West Australia (InWA), and North West Pacific (NWPa). To assist in the analysis of the

46     remaining figures in this study, Figure 6 and Table 5 briefly describe these six AAC hotspots.
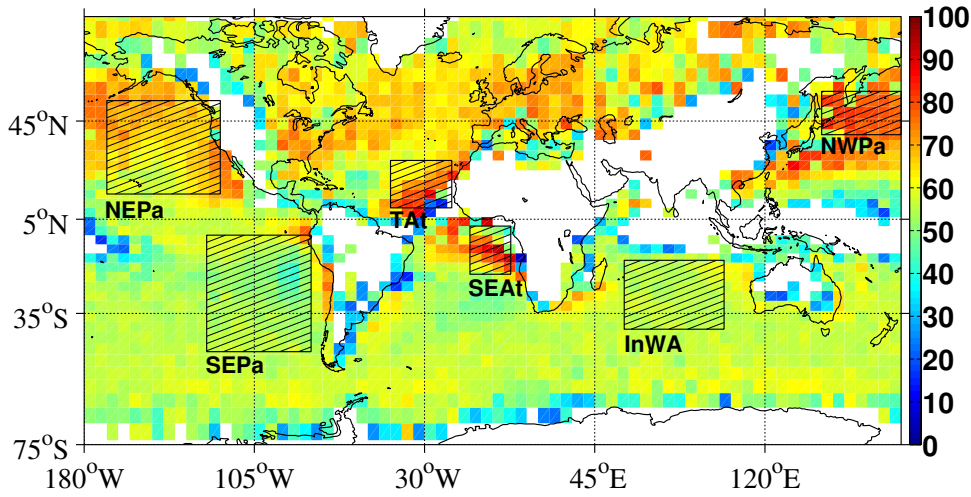
**Figure 6:** Six regions of high AAC occurrence, further defined in Table 5. Background map is the global annual 4º x 5º nighttime AAC occurrence frequency ($f_{AAC}$, see Eq. 3 and Fig. 2 for seasonal $f_{AAC}$ maps). Global annual maximum, median and mean $f_{AAC}$ values are respectively 93%, 57% and 57%.

**Table 5:** Six regions of high AAC occurrence (see Fig. 6), their season of highest AAC occurrence and its corresponding mean $f_{AAC}$ value

| Region | [latitude; longitude] | Season of most $f_{AAC}$ |
|---|---|---|
| North East Pacific Ocean (NEPa) | [16N, 52N; 170W, 120W] | MAM (80%) |
| South East Pacific Ocean (SEPa) | [49S, 2S; 126W, 80W] | DJF (55%) |
| Tropical Atlantic Ocean (TAt) | [10N, 30N; 45W, 18W] | JJA (80%) |
| South East Atlantic Ocean (SEAt) | [19S, 2N; 10W, 8E] | SON (87%) |
| Indian Ocean, offshore from West Australia (InWA) | [41S, 13S; 58E, 102E] | SON (60%) |
| North West Pacific Ocean (NWPa) | [40N, 55N; 145E, 180E] | MAM (90%) |

56    Figure 7a illustrates the mean regional, seasonal or annual estimates of SW TOA $DARE_{OWC}$ ($W·m^{-2}$) in

57    each region of Table 5. Figure 7b-7f show the primary parameters used in the $DARE_{OWC}$ calculations

58    (see section 2.2): the mean regional, seasonal or annual (b) percentage of grid cells that show valid (i.e.,

59    positive) $f_{AAC}$ x $\tau^{DR}_{AAC}$ values compared to the total number of $4º$ x $5º$ pixels in each region, (c)

60    CALIOP $f_{AAC}$ values, (d) CALIOP $f_{AAC}$ x $\tau^{DR}_{AAC}$ values, (e) assumed overlying SSA values at 546.3 nm

61    and (f) assumed underlying COD values from MODIS.
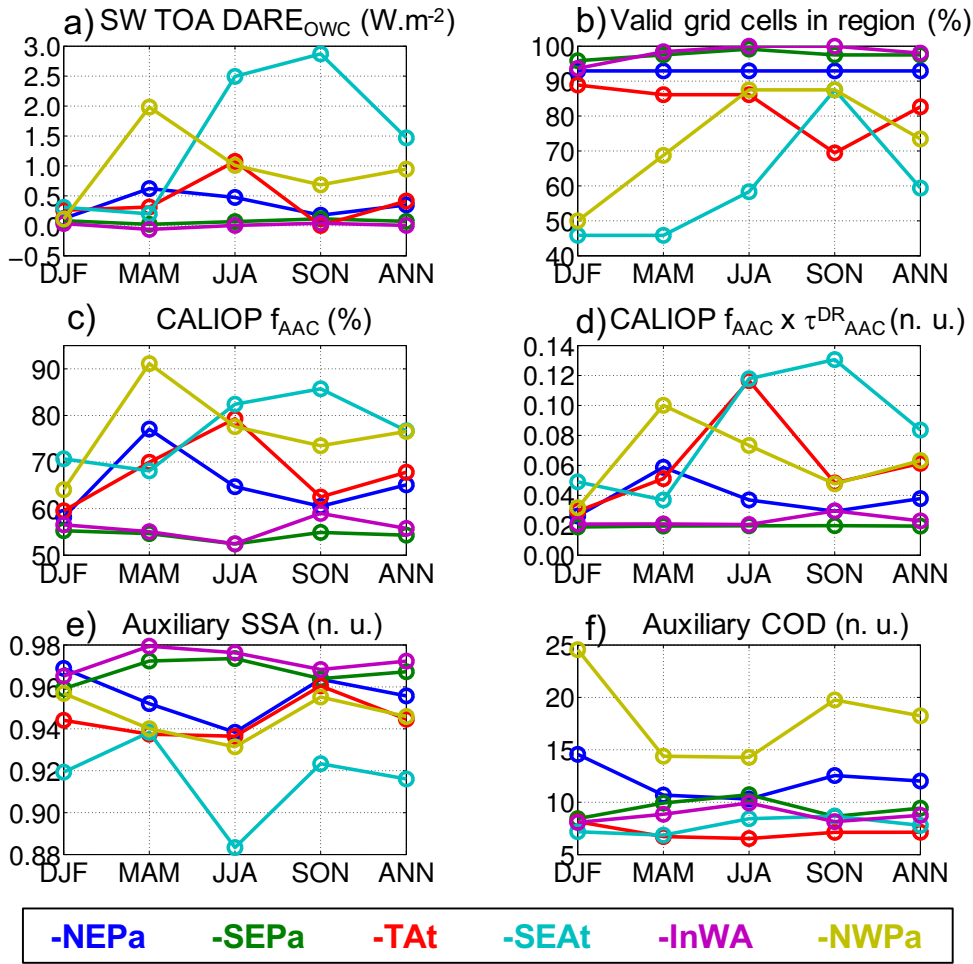
**Figure 7:** Mean regional, seasonal or annual (a) estimated SW TOA DARE$_{OWC}$ (W·m$^{-2}$, calculation is described in section 2.2), (b) percentage of grid cells that show valid f$_{AAC}$ x $\tau^{DR}_{AAC}$ (i.e., positive) values compared to the total number of 4º x 5º pixels in each region, (c) CALIOP f$_{AAC}$ (%), (d) f$_{AAC}$ x $\tau^{DR}_{AAC}$ (no unit), (e) assumed overlying SSA at 546.3 nm from a combination of MODIS-OMI-

69   CALIOP and (f) assumed underlying COD from MODIS in each region of Table 5. $DARE_{OWC}$ in (a) is

70   computed using the case IV of Table 4.

72   Table 6 reports the estimated seasonal or annual, regional range, mean and standard deviations of our

73   TOA $DARE_{OWC}$ dataset (i.e., values of Fig. 7a)

74   **Table 6:** Estimated SW TOA $DARE_{OWC}$ ($W \cdot m^{-2}$, setting is case IV of Table 4) in each region of Table

75   5.

| Region | min, max | mean DJF | mean MAM | mean JJA | mean SON | mean ANN |
|--------|----------|----------|----------|----------|----------|----------|
| NEPa | -0.57, 5.10 | 0.12±0.18 | 0.62±0.79 | 0.47±0.78 | 0.18±0.25 | 0.35 ± 0.50 |
| SEPa | -0.21, 2.85 | 0.09±0.19 | 0.02±0.15 | 0.07±0.37 | 0.12±0.44 | 0.07 ± 0.29 |
| TAt | -1.02, 5.25 | 0.26±0.43 | 0.31±0.43 | 1.08±1.66 | 0.01±0.42 | 0.41 ± 0.74 |
| SEAt | 0.20, 7.59 | 0.31±1.09 | 0.20±0.41 | 2.49±2.54 | 2.87±2.33 | 1.47 ± 1.59 |
| InWA | -0.39, 0.83 | 0.04±0.16 | -0.06±0.10 | 0.01±0.11 | 0.04±0.27 | 0.01 ± 0.16 |
| NWPa | 0.07, 5.72 | 0.11±0.14 | 1.98±1.85 | 1.01±1.65 | 0.68±0.46 | 0.95 ± 1.02 |

77   We record positive TOA $DARE_{OWC}$ values above 1 $W \cdot m^{-2}$ in Fig. 7a over TAt in JJA (1.08 ± 1.66),

78   SEAt in JJA and SON (2.49 ± 2.54 and 2.87 ± 2.33) and NWPa in MAM (1.98 ± 1.85). Let us note that

79   the highest positive TOA $DARE_{OWC}$ values on Fig. 7a and in Table 6 may not be entirely representative

80   of each region, because they are based on a smaller number of valid $DARE_{OWC}$ results (86% valid

81   values in JJA in TAt, 58-88% in JJA-SON in SEAt and 69% in MAM in NWPa). SEAt and NWPa are

82   the only regions showing an all-positive range of $DARE_{OWC}$ values in Table 6 (i.e., respectively within

83 0.20 and 7.59 and within 0.07 and 5.72 W·m$^{-2}$). The spread (i.e., standard deviation) on those mean

84 regional DARE$_{OWC}$ is of the same order of magnitude as the mean values themselves. For example,

85 although TAt shows an annual mean DARE$_{OWC}$ value of 0.41 W·m$^{-2}$, most points (i.e., about 68%,

86 assuming a normal distribution of DARE$_{OWC}$) are within 0.41 ± 0.74 W·m$^{-2}$ (see Table 6). Those regions

87 and seasons of highly positive DARE$_{OWC}$ values are associated with the highest CALIOP $\tau^{DR}_{AAC}$ x f$_{AAC}$

88 values (see Fig. 7d: 0.12 in JJA in TAt, 0.12-0.13 in JJA-SON in SEAt and 0.10 in MAM in NWPa).

89 They are also associated with lower SSA values (i.e., < 0.94 in Fig. 7e), typical of more light absorbing

90 aerosols such as biomass burning. The underlying COD values are fairly constant (between ~5-10 on

91 Fig. 7f), except for a noticeably higher COD over the NWPa region (between ~15-25 on Fig. 7f). NWPa

92 is the region of highest latitudes in our study (i.e., between 40N and 55N). More variation in the COD at

93 higher latitudes is also observed in Fig. A2 in the Appendix. This agrees with King et al. [2013], who

94 show a larger zonal variation of COD (and increased uncertainty in the MODIS cloud property

95 retrievals) in the higher latitudes of both hemispheres, particularly in winter (see their Fig. 12b).

96 When computing mean DARE$_{OWC}$ results within the "SE Atlantic" region defined in Zhang et al.

97 [2016] (i.e., [30S, 10N; 20W, 20E] instead of [19S, 2N; 10W, 8E] in our study), we find a small

98 fraction of valid pixels (i.e., an average of ~37%) but a mean annual DARE$_{OWC}$ value of 0.57 W·m$^{-2}$,

99 which resides within their range of annual DARE$_{cloudy}$ values (i.e., 0.1 to 0.68 W·m$^{-2}$ in Zhang et al.

00 [2016]). Similar to Matus et al. [2015], the season of highest DARE$_{OWC}$ is SON over the SE Atlantic

01 (they find 10% of DARE$_{OWC}$ larger than 10 W·m$^{-2}$ over thick clouds with COD > 1, see their Fig. 9d).

02 However, our DARE$_{OWC}$ results are significantly higher than the ones in Zhang et al. [2016] in our

03  SEAt region (defined as a smaller region and offshore from the "SE Atlantic" region in Zhang et al.

04  [2016]) as well as in the TAt (similar latitude/ longitude boundaries to the ones of region "TNE

05  Atlantic" in Zhang et al. [2016]) and the NWPa (similar boundaries to "NW Pacific" in Zhang et al.

06  [2016]) regions.

07  We emphasize that the $DARE_{OWC}$ estimates in this study are not directly comparable to many previous

08  studies (see Table 1) because of different spatial domain, period, satellite sensors and associated

09  uncertainties. This will lead to the detection of different fractions of AAC above different types of

10  clouds and different AAC types over the globe. The calculations of $DARE_{cloudy}$ can also differ greatly

11  depending on different AAC aerosol radiative properties assumptions above clouds (especially

12  absorption) and different assumptions in aerosol and cloud vertical heights (see Table 1).

13  Apart from the major differences in methods and sensors, it seems reasonable to say that we are missing

14  AAC cases over pure dust-dominant regions such as the Arabian Sea or the TAt region (compared to

15  e.g. Zhang et al. [2016] and Matus et al. [2015]). Both Matus et al. [2015] and Zhang et al. [2016] use

16  the CALIOP Level 2 standard products to distinguish among a few aerosol types and infer specific

17  aerosol optical properties in their $DARE_{cloudy}$. According to Figure 1(d), SEAt, TAt and the Arabian Sea

18  are regions where we might be missing up to 40% of AAC cases when using the DR technique

19  compared to the CALIOP standard products. The number of potentially missing AAC cases in our study

20  is larger over the Arabian sea ([0-30ºN and 40-80ºE] due to the limited number of OWCs suitable for

21  the DR method (see section B1 in the Appendix). Zhang et al. [2016] show that pure dust aerosols over

22  these dust-dominant regions tend to produce a negative $DARE_{cloudy}$ when the underlying COD is below

23  ~7 and this is the case for most of the clouds over these regions in their study. In summary, two factors

24  in the DR method seem to hamper the detection of AAC in these regions: the low cloud optical depths

25  of underlying clouds and very few cases of "clear air" above clouds. As a consequence, we propose that

26  the positive $DARE_{OWC}$ values in our study should, in reality, be counter-balanced by more negative

27  dust-driven $DARE_{cloudy}$ values over regions such as TAt and the Arabian Sea. On the other hand, the

28  $DARE_{cloudy}$ results from Matus et al. [2015] and Zhang et al. [2016] might also differ from the true

29  global $DARE_{cloudy}$ state of the planet for different reasons. As described in Matus et al. [2015], using

30  CALIOP Level 2 standard products as in Matus et al. [2015] and Zhang et al. [2016] could lead to

31  possible misclassification of dust aerosols as clouds [Omar et al., 2009], specifically around cloud edges

32  in the TAt region. Moreover, even if the AAC is correctly detected in Matus et al. [2015] and Zhang et

33  al. [2016], the amount of AAC AOD might be biased low due to their use of the CALIOP Level 2

34  standard products [Kacenelenbogen et al., 2014].

35  **4.  Uncertainties in our DARE above cloud results and the path forward**

36  **4.1.     Detecting and quantifying the true amount of AAC cases**

37  Our study uses mainly CALIOP Level 1 measurements to detect aerosols above specific OWCs that

38  satisfy the criteria given in Table B2. We suggest that the number of CALIOP profiles that contain

39  aerosols over any type of cloud (instead of only OWCs in this study) should be informed by a

40  combination of different techniques applied to CALIOP observations (e.g., the standard products, the

41  DR and the CR technique). Airborne observations such as those from the ObseRvations of Aerosols

42 above Clouds and their intEractionS (ORACLES) field campaigns [Zuidema et al., 2016] are well

43 suited for providing further guidance on when to apply which technique.

44 To the best of our knowledge, the true global occurrence of aerosols above any type of cloud remains

45 unknown. This question cannot be entirely answered with the use of CALIOP observations only. We

46 suggest that a more complete global quantification and characterization of aerosol above any type of

47 cloud should be informed by a combination of AAC retrievals from CALIOP, passive satellite sensors

48 (e.g. POLDER [Waquet et al., 2013a,b, Peers et al., 2015, Deaconu et al., 2017] and MODIS [Meyer et

49 al., 2013, Zhang et al., 2014, 2016], see Table 2) and model simulations [Schulz et al., 2006].

50 ### 4.2. Considering the diurnal variability of aerosol and cloud properties

51 While we consider the diurnal cycle of solar zenith angles in our $DARE_{cloudy}$ calculations, we use

52 MODIS for underlying COD and cloud $R_e$ information as well as a combination of MODIS, OMI and

53 CALIOP for overlying aerosol properties (see section 2.2). By using A-Train satellite observations (i.e.,

54 the AQUA, AURA and CALIPSO platforms), with an overpass time of 1:30 PM local time at the

55 Equator, we are only using a daily snapshot of cloud and aerosol properties and not considering their

56 daily variability.

57 Min and Zhang [2014] show a strong diurnal cycle of cloud fraction over the SEAt region (i.e., a 5-year

58 mean trend of diurnal cloud fraction using SEVIRI that varies from ~60% in the late afternoon to 80%

59 in the early morning on their Fig. 4). According to Min and Zhang [2014] (see their Table 2), assuming

60 a constant cloud fraction derived from MODIS/ AQUA generally leads to an underestimation (less

61 positive) by ~16% in the $DARE_{all-sky}$ calculations (see Eq. 1). Further studies should explore the

62    implications of diurnal variations of COD and cloud $R_e$ on $DARE_{cloudy}$ results using, for example,

63    geostationary observations from SEVIRI.

64    Daily variations of aerosol (intensive and extensive) radiative properties above clouds cannot be

65    ignored either. Arola et al. [2013] and Kassaniov et al. [2013] both show that even when the AOD

66    strongly varies during the day, the accurate prediction of 24h-average $DARE_{non\text{-}cloudy}$ requires only daily

67    averaged properties. However, in the case of under-sampled aerosol properties, such as when using A-

68    Train derived aerosol properties (this study), the error in the 24h-$DARE_{non\text{-}cloudy}$ can be as large as 100%

69    [Kassaniov et al., 2013]. Xu et al. [2016] show that the daily mean TOA $DARE_{non\text{-}cloudy}$ is overestimated

70    by up to 3.9 W·m$^{-2}$ in the summertime in Beijing if they use a constant MODIS/ AQUA AOD value,

71    compared to accounting for the observed hourly-averaged daily variability. Kassaniov et al. [2013]

72    propose that using a simple combination of MODIS TERRA and AQUA products would offer a

73    reasonable assessment of the daily averaged aerosol properties for an improved estimation of 24h-

74    $DARE_{non\text{-}cloudy}$.

75    **4.3.     Considering the spatial and temporal variability of cloud and aerosol fields**

76    We have used coarse resolution (i.e., 4º×5º) seasonally gridded aerosol and cloud properties in our

77    $DARE_{OWC}$ calculations (see section 2.2). As a consequence, sub-grid scale variability (or heterogeneity)

78    of cloud and aerosol properties has not been considered. This approach is similar to assuming spatially

79    and temporally homogeneous cloud and aerosol fields in our $DARE_{OWC}$ results.

80    Marine Boundary Layer (MBL) clouds show significant small-scale horizontal variability [Di Girolamo

81    et al., 2010; Zhang et al., 2011]. Using mean gridded COD in $DARE_{cloudy}$ calculations, for example, can

82    lead to significant biases in $DARE_{cloudy}$ calculations, an effect called the "plane-parallel albedo bias"

83    [e.g., Oreopoulos et al., 2007, Di Girolamo et al., 2010, Zhang et al., 2011, Zhang et al., 2012]. Min and

84    Zhang [2014] show that using a mean gridded COD significantly overestimates (by ~10% over the

85    SEAt region) the $DARE_{cloudy}$ results when the cloud has significant sub-grid horizontal heterogeneity.

86    Furthermore, this overestimation increases with increasing AOD, COD and cloud inhomogeneity.

87    Future studies should examine the difference between $DARE_{cloudy}$ results calculated with gridded mean

88    COD and cloud $R_e$ values (this study) and $DARE_{cloudy}$ results calculated with MODIS Level-3 joint

89    histograms of MODIS COD and cloud $R_e$ (e.g., similar to Min and Zhang [2014]).

90    Aerosol spatial variation can be significant over relatively short distances of 10 to 100km, depending on

91    the type of environment [Anderson et al., 2003; Kovacs, 2006; Santese et al., 2007; Shinozuka and

92    Redemann, 2011; Schutgens et al., 2013]. Shinozuka and Redemann [2011] argue that only a few

93    environments can be more heterogeneous than the Canadian phase of the ARCTAS (Arctic Research of

94    the Composition of the Troposphere from Aircraft and Satellites) experiment where the airmass was

95    subject to fresh local biomass emissions. In this type of environment, they observed a 19% variability of

96    the AOD over a 20 km length (comparable in scale to a ~0.1°x0.1° area). They also found a 2%

97    variability in the AOD over the same length in a contrasting homogeneous environment that occurred

98    after a long-range aerosol transport event.   As a consequence, similar to using a mean gridded

99    underlying COD and cloud $R_e$, using mean gridded overlying aerosol radiative properties could very

00    well bias our $DARE_{OWC}$ results.

01  As a preliminary investigation into the sources and magnitudes of these potential biases, we have used

02  TOA $DARE_{non-cloudy}$ (see Eq. 1) estimates derived using well-collocated aerosol properties (hereafter

03  called "retrieve-then-average" or R-A) from a companion study (Redemann et al. [2019]; see section A

04  of the appendix) and compared those to $DARE_{non-cloudy}$ estimates computed using seasonally gridded

05  mean aerosol properties at seasonally gridded mean vertical heights (hereafter called "average-then-

06  retrieve" or A-R). Both $DARE_{non-cloudy}$ results obtained with the two methods are compared over ocean

07  and at a resolution of 4ºx5º.

08  A majority (i.e., ~58%) of A-R $DARE_{non-cloudy}$ results are within ±35% of the R-A $DARE_{non-cloudy}$

09  results. We find very few (i.e., ~1%) negative R-A $DARE_{non-cloudy}$ values paired with positive A-R

10  $DARE_{non-cloudy}$ values and very few large differences between both methods (i.e., less than 1% of the

11  differences are above $\pm10W$ m$^{-2}$). However, we find a weak agreement between A-R and R-A

12  $DARE_{non-cloudy}$ values during each of the seasons (i.e., a correlation coefficient between 0.21 and 0.34).

13  The A-R $DARE_{non-cloudy}$ values are generally biased high relative to the R-A calculations, as illustrated

14  by positive mean and median values of the A-R to R-A differences (respectively 0.64 W m$^{-2}$ and 0.92

15  W m$^{-2}$; standard deviation of 2.25). When computing the global seasonal mean A-R and R-A $DARE_{non-}$

16  $_{cloudy}$ values separately, we find that the global seasonal A-R $DARE_{non-cloudy}$ values overestimate the

17  global seasonal R-A $DARE_{non-cloudy}$ values by 17%, 19%, 21%, and 17% in DJF, MAM, JJA and SON.

18  Moreover, the seasonal median A-R $DARE_{non-cloudy}$ values overestimate the seasonal median R-A

19  $DARE_{non-cloudy}$ values in all six regions of Table 5 (i.e., median differences between 0.28 W m$^{-2}$ in

20  NWPa in SON and 3.05 W m$^{-2}$ in SEAt in JJA). The geospatial distributions of these differences in

21  DARE calculation strategies are illustrated in Figure 8.

**Figure 8:** Seasonal maps showing the differences in SW TOA DARE_{non-cloudy} computed using the average-then-retrieve (A-R) and the retrieve-then-average (R-A) strategies. Positive values (in red) show regions where the A-R DARE calculations are larger, whereas negative values (in blue) show regions where the R-A DARE calculations are larger. The squares show different regions defined in Table 5. The title of each map shows the global minimum, maximum, median and mean values.

## 4.4. Assuming similar intensive aerosol properties above clouds and in near-by cloud-free skies
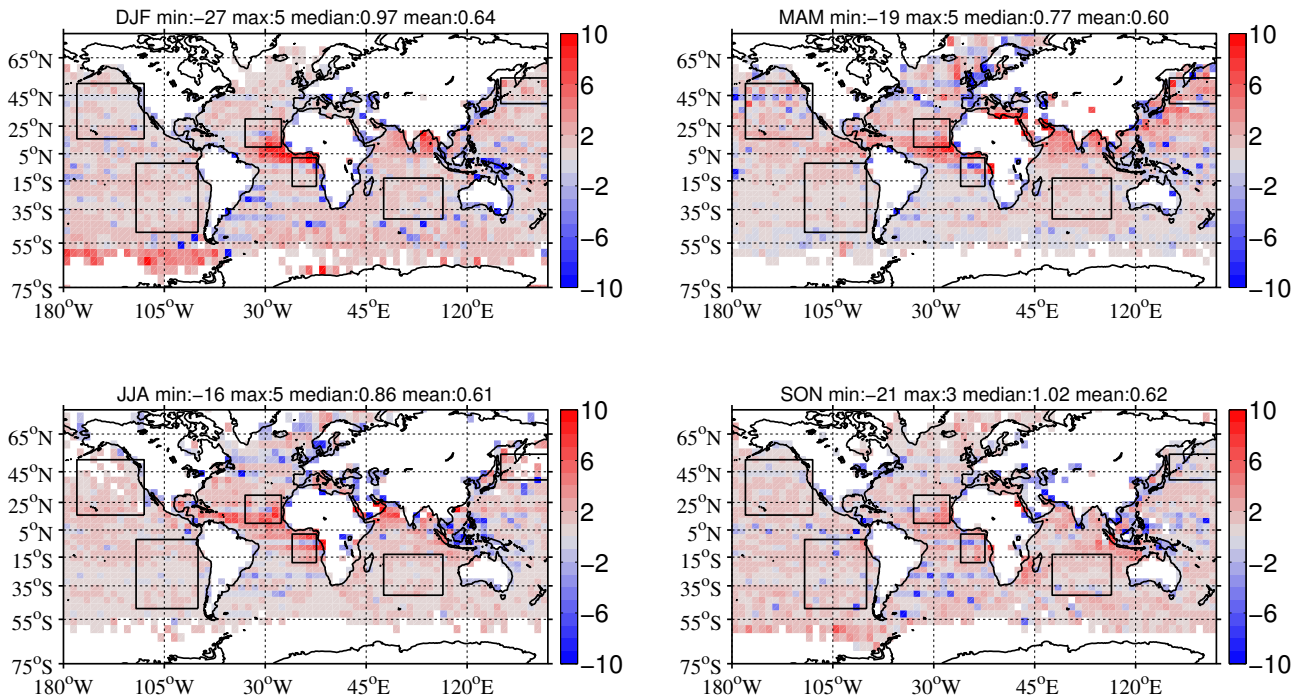
33    In the calculation of DARE$_{OWC}$, we assume similar intensive aerosol properties above clouds and in

34    near-by clear skies. This assumption might not be valid and should be investigated in future studies by

35    comparing aerosol properties and their probability distributions over clear and cloudy conditions using

36    observations from the ORACLES field campaign.

37    **4.5.      Assuming fixed aerosol and cloud vertical layers**

38    Finally, Long Wave (LW) radiative forcing is particularly dependent on the vertical distribution of

39    aerosols, especially for light absorbing aerosols [Chin et al., 2009]. This is because the energy these

40    aerosols reradiate depends on the temperature, and hence their altitude. For example, Penner et al.

41    [2003] emphasize the importance of soot and smoke aerosol injection height in LW TOA DARE$_{all\text{-}sky}$

42    (see Eq. 1) simulations (higher injection heights tend to enhance the negative LW radiative forcing).

44    Quijano et al. [2000], Chung et al. [2005] and Chin et al. [2009] demonstrate the importance of an

45    aerosol height, in relation to a cloud height (i.e., the aerosols located above, within or below the clouds)

46    in an accurate estimation of SW TOA DARE$_{all\text{-}sky}$. Chung et al. [2005], for example, show that varying

47    the relative vertical distribution of aerosols and clouds leads to a range of global anthropogenic SW

48    TOA DARE$_{all\text{-}sky}$ from -0.1 to -0.6 W·m$^{-2}$ (using a combination of MODIS satellite, AERONET ground-

49    based observations and CTM simulations, see their Table 2).

51    However, here, we concentrate on cases of aerosol layers overlying clouds in order to compute SW

52    TOA DARE$_{cloudy}$. Aerosol and cloud layer heights are assumed constant over the globe in our study (see

53  section 2.2). Future studies should incorporate mean gridded (i.e., 4º×5º in this study)-seasonal CALIOP

54  Level 2 aerosol and cloud vertical profiles into the calculation of $DARE_{OWC}$.

55  However, constraining clouds between 2 and 3km in our study does not seem unreasonable as our AAC

56  AOD calculations using the DR method can only be applied to aerosols overlying specific low opaque

57  water clouds with, among other criteria, an altitude below 3km (see Table B2). On the other hand,

58  constraining aerosols between 3 and 4km in our study is not realistic over many parts of the globe (e.g.,

59  see Fig. 7 of Devasthale et al. [2011]). For example, over the region of South East Atlantic during the

60  ORACLES campaign, the HSRL team observed an aerosol layer located in average between 2 and 5km,

61  and overlying a cloud at an average altitude of 1.2km.

63  According to Zarzycki et al. [2010], the underlying cloud properties are orders of magnitude more

64  crucial to the computation of $DARE_{cloudy}$ than the location of the aerosol layer relative to the cloud, as

65  long as the aerosol is above the cloud. In other words, the forcing does not seem to depend on the height

66  of the aerosols above clouds as much as other parameters such as the AOD, SSA or cloud albedo.

67  Zarzycki et al. [2010] investigated this assumption and found that over low and middle clouds, forcing

68  changed by ~1-3% through the heights where the Black Carbon burden was the largest. These small

69  changes in forcing are likely products of a change in atmospheric transmission above the aerosol layer

70  [Haywood and Ramaswamy, 1998] (e.g., a change in the aerosol height is linked to a change in the

71  integrated column water vapor above the aerosol layer and this, in turn, would alter the incident solar

72  radiation).

## 5. Conclusions

75     We have computed a first approximation of global seasonal TOA short wave Direct Aerosol Radiative

76 Effects (DARE) above Opaque Water Clouds (OWCs), $DARE_{OWC}$ using observation-based aerosol and

77 cloud radiative properties from a combination of A-Train satellite sensors and a radiative transfer

78 model. Our $DARE_{OWC}$ calculations make three major departures from previous peer-reviewed results:

79 (1) they use extensive aerosol properties derived from the Depolarization Ratio, DR, method applied to

80 Level 1 CALIOP measurements, whereas previous studies often use CALIOP Level 2 standard products

81 which introduce higher uncertainties and known biases; (2) our $DARE_{OWC}$ calculations are applied

82 globally, while most previous studies focus on specific regions of high AAC occurrence such as the SE

83 Atlantic; and (3) our calculations use intensive aerosol properties retrieved from a combination of A-

84 Train satellite sensor measurements (e.g., MODIS, OMI and CALIOP).

85     Our study agrees with previous findings on the locations and seasons of the maximum occurrence of

86 AAC over the globe. We identify six regions of high AAC occurrence (i.e., AAC hotspots): South and

87 North East Pacific (SEAt and NEPa), Tropical and South East Atlantic (TAt and SEAt), Indian Ocean

88 offshore from West Australia (InWA) and North West Pacific (NWPa). We define $\tau^{DR}_{AAC}$, the Aerosol

89 Optical Depth (AOD) above OWCs using the DR method on CALIOP measurements, $f_{AAC}$, and the

90 frequency of occurrence of AAC cases. We record a majority of $\tau^{DR}_{AAC}$ x $f_{AAC}$ values at 532nm in the

91 0.01-0.02 range and that can exceed 0.2 over a few AAC hotspots.

92     We find positive averages of global seasonal $DARE_{OWC}$ between 0.13 and 0.26 W·m$^{-2}$ and an annual

93 global mean $DARE_{OWC}$ value of 0.20 W·m$^{-2}$ (i.e., a warming effect on climate). Regional seasonal

94   DARE$_{OWC}$ values range from -0.06 W·m$^{-2}$ in the Indian Ocean, offshore from western Australia (in

95   March-April-May) to 2.87 W·m$^{-2}$ in the South East Atlantic (in September-October-November). High

96   positive values are usually paired with high aerosol optical depths (>0.1) and low single scattering

97   albedos (<0.94), representative of e.g. biomass burning aerosols.

98   Although the DARE$_{OWC}$ estimates in this study are not directly comparable to previous studies because

99   of different spatial domain, period, satellite sensors, detection methods, and/ or associated uncertainties,

00   we emphasize that they are notably higher than the ones from [Zhang et al., 2016; Matus et al., 2015

01   and Oikawa et al., 2013].  In addition to differences in satellite sensors, AAC detection methods, and

02   the assumptions enforced in the calculation of DARE$_{cloudy}$, there are several other factors that may

03   contribute to the overall higher DARE$_{OWC}$ values we report in this study. The most likely contributors

04   are (1) a possible underestimate of the number of dust-dominated AAC cases; (2) our use of the DR

05   method on CALIOP Level 1 data to quantify the AAC AOD; and, in particular, (3) the technique we

06   have chosen for aggregating sub-grid aerosol and cloud spatial and temporal variability. We discuss

07   each of these in turn in the following paragraphs.

08   Two factors seem to be preventing the DR method from recording enough AAC cases in these regions:

09   the low cloud optical depths of underlying clouds and very few cases of "clear air" above clouds. The

10   DR method used in this study is restricted to aerosols above OWCs that satisfy a long list of criteria.

11   The AAC dataset in this study underestimates (i) the total number of CALIOP 5 km profiles that

12   contain AAC over all OWCs (i.e., not just suitable to the DR technique), (ii) the total number of

13   CALIOP 5 km profiles that contain AAC over any type of clouds over the globe and (iii) the true global

14   occurrence of AAC over any type of clouds. To the best of our knowledge, the true amount of AAC in

15   (i), (ii) and (iii) remains unknown. A better characterization of the "unobstructed" OWCs in the

16   application of the DR technique on CALIOP measurements might bring us closer to answering (i). A

17   combination of CALIOP standard, DR and CR techniques together with airborne observations (e.g.,

18   from the ORACLES field campaign) might answer (ii). Finally, (iii) cannot be answered with the only

19   use of CALIOP observations. The results in this study should be combined with aerosol-above-cloud

20   retrievals from passive satellite sensors (e.g. POLDER [Waquet et al., 2013a,b, Peers et al., 2015,

21   Deaconu et al., 2017] or MODIS [Meyer et al., 2013, Zhang et al., 2014, 2016]) and model simulations

22   [Schulz et al., 2006] to obtain a more complete global quantification and characterization of aerosol

23   above any type of clouds.

24   Compared to other methods, the DR technique applied to CALIOP measurements retrieves $\tau^{DR}_{AAC}$ with

25   fewer assumptions and lower uncertainties. Other global $DARE_{cloudy}$ results (e.g., Matus et al. [2015]

26   and Zhang et al. [2016]) use CALIOP standard products to detect the AAC cases, quantify the AAC

27   AOD and define the aerosol type (and specify the aerosol intensive properties). These studies rely on

28   the presence of aerosol in concentrations sufficient to be identified by the CALIOP layer detection

29   scheme, and on the ability of the CALIOP aerosol subtyping algorithm to correctly identify the aerosol

30   type and thus select the correct lidar ratio for the AOD retrieval.  While several recent studies have

31   taken various approaches to quantifying the amount of aerosol currently being undetected in the

32   CALIOP backscatter signals, their general conclusions are unanimous. The CALIOP standard products

33   underestimate above-cloud aerosol loading and the corresponding AAC AOD (Kacenelenbogen et al.,

34    2014; Kim et al., 2017; Toth et al., 2018; Watson-Parris et al., 2018), and this in turn leads to

35    underestimates of both $DARE_{non-cloudy}$ and $DARE_{cloudy}$ (Thorsen and Fu, 2015; Thorsen et al., 2017).

36    In this study, we have assumed spatially and temporally homogeneous clouds and aerosols in our

37    $DARE_{OWC}$ calculations. As a preliminary investigation of such effects on our calculations, we have

38    compared DARE calculations derived from well collocated aerosol properties (retrieve-then-average) to

39    DARE calculations using seasonally gridded mean aerosol properties (average-then-retrieve). We have

40    shown that the average-then-compute DARE results generally overestimate the retrieve-then-average

41    results both on a global scale and in each of our selected regions. Further research and analysis are

42    required to determine which of these two computational approaches provides the most accurate

43    estimates of real-world DARE.

**Appendix A: Method to obtain aerosol radiative properties in non-cloudy (i.e., clear-sky)**

**conditions using MODIS, OMI and CALIOP and to estimate DARE$_{non-cloudy}$**

48 A companion paper, Redemann et al. [2019], develops and refines a method for retrieving full spectral

49 (i.e., at 30 different wavelengths) extinction coefficients, Single Scattering Albedo (SSA) and

50 asymmetry parameters from satellite aerosol products in non-cloudy (i.e., clear-sky) conditions. The

51 method requires colocation of quality-screened satellite data, selection of aerosol models that reproduce

52 the satellite observations within stated uncertainties, and forward calculation of aerosol radiative

53 properties based on the selected aerosol models. They use MODIS-Aqua AOD at 550 and 1240 nm,

54 CALIPSO integrated backscattering (IBS) at 532 nm and OMI Absorption Aerosol Optical Depth

55 (AAOD) at 388 nm (see Table A1). The aerosol radiative properties resulting from this method are

56 called MOC retrievals (for MODIS-OMI-CALIOP).

Table A1. Data sets currently used for global MODIS-OMI-CALIOP (MOC) retrievals of aerosol radiative properties [Redemann et al., 2019]; DT: Dark Target and EDB: Enhanced Deep Blue.

| Product | Source | Assumed Uncertainties* | Weight*,** |
|---|---|---|---|
| 550 nm AOD | MODIS Collection 6 (Ocean, DT-Land, EDB-Land) | $\pm 5\% \pm 30$ Mm$^{-1}$ | 0.1488 |
| 1240 nm AOD | MODIS Collection 6 (extrapolated spectrally over land) | $\pm 5\% \pm 30$ Mm$^{-1}$ | 0.1422 |
| 388 nm AAOD | OMI (OMAERO for ocean, OMAERUV for DT-land), MODIS EDB | $\pm 30\% \pm 50$ Mm$^{-1}$ | 0.5542 |
| 532 nm IBS | CALIPSO V3-01 | $\pm 30\% \pm 0.1$ Mm$^{-1}$sr$^{-1}$ | 0.1548 |

\* For the values after division by CALIPSO layer depth

\*\* The weight, $w_i$, is used to calculate the cost function $X = (\Sigma w_i((x_i - \hat{x}_i)/\hat{\delta x}_i)^2)^{1/2}$ where $x_i$ are the retrieved parameters, $\hat{x}_i$ are the observables, $\hat{\delta x}_i$ are the uncertainties in the observables.

The choice of OMI satellite algorithms (see Table A1) reflects their assessment of the representativeness of subsampling OMI data along the CALIPSO track; i.e., they compared the probability distribution (PDF) of the OMI retrievals along the CALIPSO track to the global PDF and chose the data set that had the best match between global and along-track PDF for the over-ocean and two over-land data sets, the latter being different in their use of MODIS dark target (DT) versus enhanced Deep-Blue (EDB) data as the source of AOD. They collocate the MODIS and OMI products within a 40x40 km$^2$ box centered at each CALIPSO 5-km profile location after Redemann et al. [2012].

71    For the OMAERUV data set, they choose the SSA product for the layer height indicated by the

72    collocated CALIOP backscatter profile.

73    Their aerosol models emulate those of the MODIS aerosol over-ocean algorithm [Remer et al., 2005].

74    Like the MODIS algorithm, they define each model with a lognormal size distribution and wavelength-

75    dependent refractive index. They then combine two of these models, weighted by their number

76    concentration, and compute optical properties for the bi-modal lognormal size distribution. Unlike the

77    MODIS algorithm, they allow combinations of two fine-mode or two coarse-mode models. They use

78    ten different aerosol models, which stem from some of the MODIS over-ocean models [Remer et al.,

79    2005] but include more absorbing models, which was motivated by application of their methodology to

80    the Arctic Research of the Composition of the Troposphere from Aircraft and Satellites (ARCTAS)

81    field campaign data, requiring more aerosol absorption than included in the current MODIS over-ocean

82    aerosol models. They use MOC spectral aerosol radiative properties to then calculate Direct Aerosol

83    Radiative Effects (i.e., $DARE_{non-cloudy}$, see Eq. 1) through a delta-four stream radiative transfer model

84    with fifteen spectral bands from 0.175 to 4.0 μm in SW and twelve longwave (LW) spectral bands

85    between 2850 and 0 $cm^{-1}$ [Fu and Liou, 1992].

86    In order to use these MOC parameters (retrieved in clear-skies) in our $DARE_{OWC}$ calculations, we need

87    to assume similar aerosol intensive properties in clear skies compared to above clouds and we need to

88    spatially and/ or temporally grid these MOC parameters. As discussed in section 2.2, we use seasonally

89    averaged MOC spectral SSA, aerosol asymmetry parameter, and extinction retrievals on 4ºx5º grids.

90    Figure A1 illustrates seasonal maps of MOC SSA used in our calculations of $DARE_{OWC}$.

92
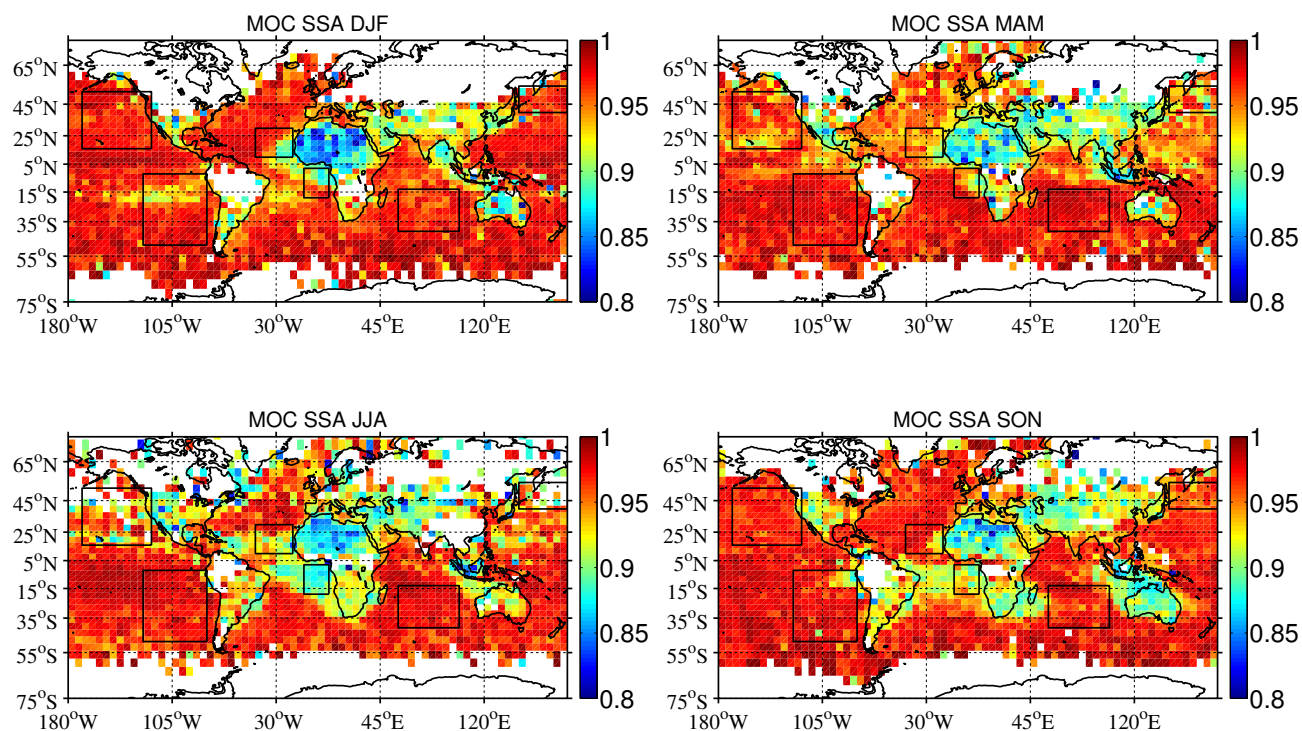
Figure A1: Seasonal maps of MOC SSA at 546.3 nm in 2007 used in the calculations of $DARE_{OWC}$. The squares show different regions defined in Table 5.

The $DARE_{OWC}$ calculations in our study also require information about the underlying cloud optical properties. As discussed in section 2.2, we use seasonally mean gridded COD from MODIS such as illustrated in Figure A2.
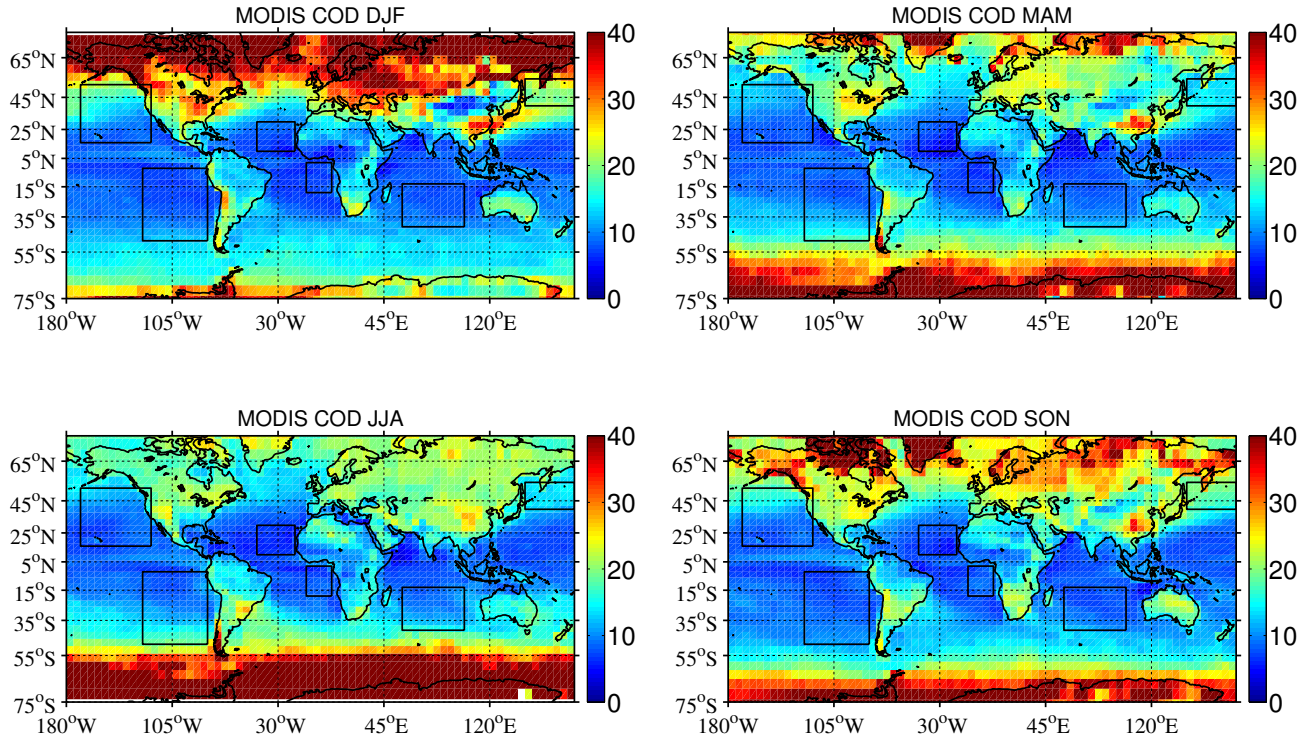
Figure A2: Seasonal maps of COD used in the calculations of DARE$_{OWC}$. COD information is inferred from MODIS seasonally averaged monthly 1°x1° grids (i.e. liquid water cloud products of MYD08_M3: "Cloud Effective Radius Liquid Mean Mean" and "Cloud Optical Thickness Liquid Mean Mean" [Platnick et al. 2015]) from 2008 to 2012. The squares show different regions defined in Table 5.

**Appendix B: Method for AAC detection and AAC AOD computation**

The depolarization ratio (DR) method [Hu et al., 2007b] used to derive estimates of the optical depths (τ) of aerosols above clouds (AAC) is given in Eq. (2) and repeated here for convenience:

$$\tau^{DR}_{AAC} = -0.5 \times \ln[IAB^{OWC}_{SS,AAC} / IAB^{OWC}_{SS,CAC}] \tag{B1}$$

10   The subscripts SS and CAC represent, respectively, 'single scattering' and 'clear above clouds'.

11   $IAB^{OWC}_{SS}$ (i.e., either $IAB^{OWC}_{SS,AAC}$ or $IAB^{OWC}_{SS,CAC}$) is the single scattering integrated attenuated

12   backscatter (IAB), derived from the product of the measured 532 nm attenuated backscatter coefficients

13   integrated from cloud top to cloud base, $IAB^{OWC}$, and a layer effective multiple scattering factor, $\eta^{OWC}$,

14   derived from the layer-integrated volume depolarization ratio of the water cloud (called $\delta^{OWC}$) using:

15   $\eta^{OWC} = [(1-\delta^{OWC})/(1+\delta^{OWC})]^2$                                        (B2)

16   [Hu et al., 2007a]. The single scattering IAB is thus derived using:

17   $IAB^{OWC}_{SS,X} = \eta^{OWC} \times IAB^{OWC}_{measured,X}$                              (B3)

18   for both aerosol above cloud cases (X = AAC) and those cases with clear skies above (X = CAC). An

19   assumption of the DR method is that $\delta^{OWC}$ is negligibly affected by any aerosols that lie in the optical

20   path between the OWC and the lidar.

21   Table B1 provides a high-level overview of the procedure we use to compute aerosol optical depth

22   ($\tau^{DR}_{AAC}$) above OWCs over the globe. We chose to concentrate on night-time CALIOP observations

23   only, as they have substantially higher signal-to-noise ratios (SNR) than the daytime measurements

24   [Hunt et al., 2009].

26   **Table B1:** Steps required to compute $\tau^{DR}_{AAC}$. (*): we construct global maps of 4 x 5° pixels using

27   median values. Superscripts 1 and 2 denote respectively CALIOP Level 1 and Level 2 aerosol or cloud

28   layer products.

| Step | Description | CALIOP, GEOS-5 and other computed products that are used in each step | More detail |
|---|---|---|---|
| S1 | Select specific Opaque Water Clouds (OWC) suitable for the DR technique | CAD Score[2], Integrated Attenuated Backscatter Uncertainty 532[2], Integrated Volume Depolarization Ratio Uncertainty[2], Horizontal Averaging, Opacity Flag[2], Feature Classification Flags[2], Layer Top Altitude[2], Layer Top Temperature[2], Surface Wind Speed[2] | section B1, Table B2 |
| S2 | Select a subset of OWCs from (S1) with clear air above | Overlying Integrated Attenuated Backscatter 532[2], simulated molecular layer-integrated attenuated backscatter [Powell et al., 2002 and 2006] and OWCs from (S1) | section B2 |
| S3 | Process seasonal maps of median $IAB^{OWC}_{SS,CAC}$ and record number of $IAB^{OWC}_{SS,CAC}$ values per grid cell [*] | Integrated Attenuated Backscatter 532[2], Integrated Volume Depolarization Ratio[2], and OWCs with clear air above from (S2) | section B3 |
| S4 | Compute $\tau^{DR}_{AAC}$ along track | Total Attenuated Backscatter 532[1], Molecular Number Density[1], Ozone Number Density[1] Integrated Attenuated Backscatter 532[2,+], Integrated Volume Depolarization Ratio[2,+], Layer Top Altitude[2,+], Layer Base Altitude[2,+] and seasonal maps of $IAB^{OWC}_{SS,CAC}$ from (S3) Note: [+] these parameters are re-computed from CALIOP level 1 data, and may differ from the standard CALIOP products | Eq. (2) or Eq. (B1) |
| S5 | Process seasonal maps of median $\tau^{DR}_{AAC}$ and record number of $\tau^{DR}_{AAC}$ values per grid cell [*] | $\tau^{DR}_{AAC}$ of (S4) and we filter using number of $IAB^{OWC}_{SS,CAC}$ values per grid cell and per season from (S3) | Results in section 3.2 |

The first step (S1) is to identify OWCs that are suitable for the application of the DR method. The
acceptance criteria used to identify these clouds are described below in section B1 and listed in Table
B2. In the second step (S2), we use the overlying integrated attenuated backscatter (i.e., the 532 nm

33    attenuated backscatter coefficients integrated from TOA to the OWC cloud tops) to partition the OWC

34    into two classes: (i) "unobstructed" clouds, for which the magnitude of the overlying IAB suggests that

35    only aerosol-free clear skies lie above; and (ii) "obstructed" clouds for which we expect to be able to

36    retrieve positive estimates of $\tau^{DR}_{AAC}$. Section B2 describes the objective method we have developed to

37    separate unobstructed clouds (for which we can compute $IAB^{OWC}_{SS,CAC}$) from obstructed clouds (for

38    which we calculate $IAB^{OWC}_{SS,AAC}$).

39    In step (S3), we construct global seasonal maps of median $IAB^{OWC}_{SS,CAC}$ using 5 consecutive years

40    (2008-2012) of CALIOP nighttime data (see section B3). By doing this we can subsequently compute

41    estimates of $\tau^{DR}_{AAC}$ without invoking assumptions about the lidar ratios of water clouds in clear skies

42    [Hu et al., 2007]. Throughout this study, we chose to compute global median values within each grid

43    cell (instead of mean values) to limit the impact of particularly high or low outliers on our statistics.

44    In step (S4), we compute estimates of $\tau^{DR}_{AAC}$ for all obstructed OWC within each grid cell using Eq. (2)

45    or Eq. (B1) and the 5-year nighttime seasonal median values of $IAB^{OWC}_{SS,CAC}$ from (S3) (i.e., each

46    $\tau^{DR}_{AAC}$ value along the CALIOP track is computed using one median value of $IAB^{OWC}_{SS,CAC}$ per 4º x5º

47    pixel and per season).

48    For the OWCs considered in this study, true layer base cannot be measured by CALIOP, simply

49    because the signal becomes totally attenuated at some point below the layer top. Instead, what is

50    reported in the CALIOP data products is an apparent base, which indicates the point at which the signal

51    was essentially indistinguishable from background levels. Numerous validation studies have established

52    the accuracy of the CALIOP cloud layer detection scheme (e.g., McGill et al., 2007; Kim et al., 2011;

53  Thorsen et al., 2011; Yorks et al., 2011; Candlish et al., 2013). Strong attenuation of the signal by

54  optically thick aerosols above an OWC can, in some cases, introduce biases into the cloud height

55  determination, which would lead to misestimates of $IAB^{OWC}_{SS,AAC}$ and subsequent errors in $\tau^{DR}_{AAC}$. To

56  ensure the use of consistent data processing assumptions throughout our retrievals of $\tau^{DR}_{AAC}$, we

57  recalculated the components of $IAB^{OWC}_{SS,AAC}$ (i.e., the "Integrated Attenuated Backscatter 532" and

58  "Integrated Volume Depolarization Ratio") using parameters in the CALIOP Level 1 product ("Total

59  Attenuated Backscatter 532", "Molecular Number Density" and "Ozone Number_Density") and

60  optimized estimates of cloud top and base altitudes based on the "Layer Top Altitude" and "Layer Base

61  Altitude" values reported in the CALIOP Level 2 layer product.

62  Apart from the identification of specific OWCs in step (S1), the primary Level 2 CALIOP parameters

63  used to calculate $\tau^{DR}_{AAC}$ (S2-S4 in Table B1) are (i) the integrated attenuated backscatter above cloud

64  top to detect "clear air" cases (i.e. "Overlying Integrated Attenuated Backscatter 532" in step (S2)), (ii)

65  the layer integrated attenuated backscatter of the OWC with clear air above (i.e. "Integrated Attenuated

66  Backscatter 532" in step (S3)) and (iii) the cloud multiple scattering factor, derived as a function of the

67  layer integrated volume depolarization ratio (i.e. the "Integrated Volume Depolarization Ratio" in S3

68  and S4).

69  Below, we list the potential sources of errors associated with those three products:

70  (a) the accuracy of the 532 nm channel calibrations,

71  (b) the signal-to-noise ratio (SNR) of the backscatter data within the layer,

72  (c) the estimation of molecular scattering in the integrated attenuated backscatter (section 3.2.9.1 of the

73   CALIPSO   Feature   Detection   ATBD,   http://www-calipso.larc.nasa.gov/resources/pdfs/PC-SCI-

74   202_Part2_rev1x01.pdf), and

75   (d) the accuracy of the depolarization calibration (see section 5 in Powell et al., [2009]).

76   Concerning (a), Rogers et al. [2011] show that the NASA LaRC HSRL and CALIOP Version 3 532 nm

77   total attenuated backscatter agree on average within ~3%, demonstrating the accuracy of the CALIOP

78   532 nm calibration algorithms.

79   Concerning (b), we assume the influence of the SNR returned from the OWC is negligible as the OWCs

80   are strongly scattering features and our dataset is composed of nighttime data only. However, the

81   backscatter from tenuous and spatially diffuse aerosol layers with large extinction-to-backscatter ratios

82   can lie well beneath the CALIOP attenuated backscatter detection threshold.  When such layers lie

83   above OWCs, the measured overlying integrated attenuated backscatter can fall within one standard

84   deviation of the expected 'purely molecular' value that is used to identify CAC (or "unobstructed")

85   OWC in our dataset (S2; see Sect. B2). Within the context of this study, these tenuous and spatially

86   diffuse aerosol layers can have appreciable AOD, and thus care must be taken to ensure that these sorts

87   of cases are not misclassified as CAC OWC. Section B3 discusses such cases, possibly found, for

88   example, over the region of SEAt.

90   **B1. Select specific Opaque Water Clouds suitable for DR technique**

91    Successful application of the DR method (Eq. 2 or Eq. B1) requires a very specific type of underlying

92    cloud (step (S1) in Table B1). Table B2 lists the criteria we have applied to the CALIOP 5 km cloud

93    layer products for the selection of these specific OWCs over the globe.

94

95    **Table B2:** Criteria used to select the Opaque Water Clouds (OWC) for the application of the DR

96    method to obtain the AAC frequency of occurrence, AAC optical depth, AAC lidar ratio and $DARE_{OWC}$

97    in this study.

| criteria | metric | interpretation |
|---|---|---|
| C1 | Number of cloud layers = 1 | a single cloud in each column |
| C2 | High CALIOP cloud-aerosol discrimination (CAD) score ($90 \leq CAD \leq 100$) and high SNR (IAB SNR $> 159$, $\delta^{OWC}$ SNR $> 2$) | highly confident of cloud classification |
| C3 | Cloud detected at 5 km averaging resolution with CALIOP single shot cloud cleared fraction = 0 | cloud is spatially uniform over a 5 km averaging interval |
| C4 | CALIOP opacity flag = 1; surface wind speed < 9 m/s | cloud is opaque |
| C5 | CALIOP phase classification is high confidence water; $\delta^{OWC} < 0.5$; cloud top altitude < 3 km; cloud top temperature $\geq$ -10° C | highly confident of cloud phase identification (water) |

98    We ensure that each cloud is the only cloud detected within the vertical column (C1) and is guaranteed

99    to be of high quality by imposing filters on various CALIOP quality assurance flags (C2). Imposing the

00    "single shot cloud cleared fraction = 0" in criterion (C3) assures that the clouds are uniformly detected

01    at single shot resolution throughout the full 5 km (15 shot) horizontal extent. As a result, we will

02    intentionally miss any broken clouds and any clouds that show a weaker scattering intensity within one

03    or more laser pulses with the 15 shot average. On the other hand, enforcing the single shot cloud

04    fraction = 0 criteria simultaneously ensures that all $\tau^{DR}_{AAC}$ values in this study will lie below a certain

05    threshold: larger values would attenuate the signal to the point that single shot detection of underlying

06    clouds is no longer likely. Consequently, some highly attenuating biomass burning events (e.g., with

07    $\tau^{DR}_{AAC}$ >2.5) can be excluded from the cases considered here.

08    At high surface wind speeds over oceans, the CALIOP V3 layer detection algorithm may fail to detect

09    surface backscatter signals underneath optically thick but not opaque layers. In such cases, CALIOP's

10    standard algorithm may misclassify the column as containing an opaque overlying cloud. To avoid such

11    scenarios, we exclude all the cases with high surface wind conditions (C4). Let us note that this

12    condition was applied on the entire dataset, disregarding the surface type (i.e. land or ocean), as our

13    OWC dataset resides mostly over ocean surfaces (see Figure 1b).

14    Criterion (C5) requires that the OWC be both low enough (cloud top below 3km) and warm enough

15    (cloud top temperature above -10ºC as in Zelinka et al. [2012]) to ensure that it is composed of liquid

16    water droplets. After applying all the criteria of Table B2, the median OWC top height of our dataset is

17    ~1.6 km. According to Hu et al. [2009], any feature showing a cloud layer integrated volume

18    depolarization ratio above 50% should correspond to an ice cloud with randomly oriented particles.

19    Criterion (C5) assures the deletion of such cases.

20    The averaged single-layer, high QA, uniform cloud (i.e. C1-C3 in Table B2) has a top altitude of ~8

21    km, a top temperature around -38º C and mean surface winds of ~6 m s$^{-1}$. Selecting only those clouds

22    with top temperatures above -10º C removes 30-40% of the observations. Subsequently filtering out

23    clouds with top heights above 3 km removes an additional 30% of the observations. Finally, filtering

24    out clouds with underlying winds above 9 m s$^{-1}$ deletes another 20% of the observations. Among all

25    single-layer, high QA, uniform clouds (i.e. C1-C3 in Table B2), we find that ~45-50% are opaque

26    clouds (C4), and that ~11-12% satisfy all criteria (C1-C5) of Table B2.

28    **B2. Select a subset of Opaque Water Clouds with clear air above**

29    To distinguish between OWCs having clear skies above (i.e., unobstructed clouds, see S2 in Table B1)

30    and those having overlying aerosols, we examine the overlying integrated attenuated backscatter

31    reported in the CALIOP Level 2 cloud layer products. The total Integrated Attenuated Backscatter

32    (IAB) value above a cloud (i.e., $IAB^{tot}_{aboveCloud}$) can be written as follows:

33    $$IAB^{tot}_{aboveCloud} = \int_0^{cloudtop} \left[ \beta_a(r) T_a^2(0,r) T_m^2(0,r) \right] dr + \int_0^{cloudtop} \left[ \beta_m(r) T_m^2(0,r) T_a^2(0,r) \right] dr \qquad (B4)$$

34    Here $\beta_a(r)$ and $\beta_m(r)$ are, respectively, the aerosol and the molecular backscatter coefficients (km$^{-1}$ sr$^{-1}$)

35    at range r (km), and $T_a^2(0,r)$ and $T_m^2(0,r)$ are the two-way transmittances between the lidar (at range r =

36    0) and range r due to, respectively, aerosols and molecules.

37    Figure B1 shows simulated profiles of the integrated attenuated backscatter above any given altitude, z,

38    ($IAB^{mol}_{above\ z}$) for a purely molecular atmosphere for both daytime (solid green curve) and nighttime

39    conditions (dashed green curve). These data were generated by the CALIPSO lidar simulator [Powell et

40    al., 2002; Powell, 2005; Powell et al., 2006] using molecular and ozone number density profiles

41  obtained from the GEOS-5 atmospheric data products distributed by the NASA Goddard Global

42  Modeling and Assimilation Office (GMAO). The error envelopes at ±1 standard deviation (light blue

43  curves) and ±1.5 standard deviation (dark blue curves) around the mean represent measurement

44  uncertainties for CALIPSO profiles averaged to a nominal horizontal distance of 5 km.  The mean

45  $IAB^{mol}_{above\ z}$ profiles represent an average of all data along the CALIPSO orbit track on 17 March 2013

46  that began at 03:29:28 UTC and extended from 78.8°N, 20.3°E to 77.3°S, 77.0°W.  Spot checks of

47  mean $IAB^{mol}_{above\ z}$ profiles from different seasons show variations of ~10% or less, depending on

48  latitude, for altitudes of 3 km and below. The largest differences are found poleward of 30°. While the

49  daytime and nighttime mean values are, as expected, essentially indistinguishable from one another, the

50  error envelopes differ drastically due to the influence of solar background noise during daylight

51  measurements. In this study, we use nighttime measurements only.
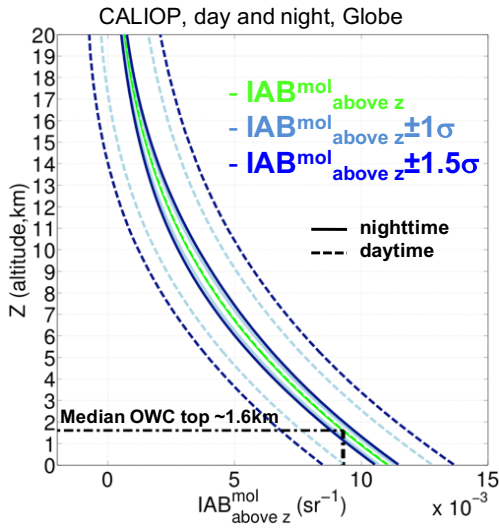
53  **Figure B1:** Nighttime (solid) and daytime (dashed) simulated vertical profile of integrated attenuated

54  backscatter above any given altitude, z, $IAB^{mol}_{above\ z}$ (green curve). The light blue (respectively dark

55    blue) envelope shows 1 (respectively 1.5) standard deviation ($\sigma$) around the $IAB^{mol}_{above\ z}$ profile. Data

56    was generated by the CALIPSO lidar simulator [Powell et al., 2002 and 2006]. The $IAB^{mol}_{above\ z}$ value

57    associated to the median OWC top height of ~1.6 km in our dataset corresponds to 0.0093 $sr^{-1}$.

59    In this study, we assume "clear air" when $IAB^{tot}_{aboveCloud}$ is within the simulated $IAB^{mol}_{aboveCloud}$ value $\pm$

60    $1\sigma$ (i.e., the light blue envelope shown in Figure B1). This definition of "clear air above" conditions is

61    somewhat more restrictive than those imposed in previous studies. For example, Liu et al. [2015]

62    conducted an extensive study of AAC optical depths and lidar ratios using CALIOP measurements over

63    the tropical and southeast Atlantic. To identify clear air above cloud cases, Liu et al. [2015] require that

64    the integrated attenuated scattering ratio, defined as

66    $$ASR = \frac{\int_{8km}^{OWC_{top}} (\beta_m(r) + \beta_a(r)) T_m^2(0,r) T_a^2(0,r) dr}{\int_{8km}^{OWC_{top}} \beta_m(r) T_m^2(0,r) dr} \hspace{2cm} (B5)$$

67    , fall within the range of $0.95 < ASR < 1.05$, irrespective of cloud top altitude. For comparison, at the

68    maximum OWC top altitude used in our analyses (3 km), $(IAB^{mol}_{aboveCloud} \pm 1\sigma) / IAB^{mol}_{aboveCloud} = 1 \pm$

69    0.0380. This restriction tightens for lower cloud top heights; e.g., at our mean OWC top altitude of 1.6

70    km, $(IAB^{mol}_{aboveCloud} \pm 1\sigma) / IAB^{mol}_{aboveCloud} = 1 \pm 0.0325$.

71    The pioneering study by Chand et al. [2008], who first used the CALIOP DR method to assess the

72    radiative effects of aerosols above clouds, took a different approach to identifying "clear above cloud"

73    cases. Rather than examining the overlying IAB, they instead assumed clear air above conditions

74 whenever $IAB^{OWC}_{SS} > 0.025$ sr$^{-1}$. As will be shown in section B3, in addition to the $IAB^{mol}_{aboveCloud}$

75 limits cited above, our study also enforces limits on $IAB^{OWC}_{SS,CAC}$. This combination of limits on both

76 $IAB^{mol}_{aboveCloud}$ and $IAB^{OWC}_{SS,CAC}$ serves to more effectively reject aerosol-contaminated profiles from

77 the "clear above" data set than either one alone.

79 **B3. Process median seasonal maps of Integrated Attenuated Backscatter of Opaque Water Clouds**

80 **showing Clear Air Above**

81 Once we select specific OWCs (i.e., that satisfy the criteria of Table B2) and define which ones are

82 "unobstructed" (see section B2), we can easily compute $IAB^{OWC}_{SS,CAC}$ by using Eq. (B3). For clouds

83 that totally attenuate the lidar signal (i.e., cloud optical depths greater than ~6 [Young et al., 2018]),

84 $IAB^{OWC}_{SS,CAC}$ in Eq. (2) or Eq. (B1) is related to the OWC lidar ratio (called $S_c$), so that

85 $S_c = 1 / (2 \times \eta^{OWC} \times IAB^{OWC}_{CAC}) = 1 / (2 \times IAB^{OWC}_{SS,CAC})$ (B6)

86 [Platt, 1973]. OWC $S_c$ values are relatively stable at the visible and near infrared wavelengths [Pinnick

87 et al., 1983, O'Connor et al., 2004], but show large variations over land [Pinnick et al., 1983; Hu et al.,

88 2006]. $S_c$ is known to vary as a function of cloud droplet microphysics, and is especially sensitive to

89 cloud droplet effective radius ($R_e$) and the imaginary part of the refractive index (see Fig. 8 of Deaconu

90 et al. [2017]). Hu et al., [2006], Liu et al. [2015] and Deaconu et al. [2017] show that a decrease of $R_e$ is

91 often paired with an increase of estimated $S_c$ at 532 nm for pure, non-aerosol-contaminated water

92 clouds (i.e., cloud droplets having an imaginary refractive index of 0).

93    As an example, Figure B3a shows the median nighttime CALIOP $S_c$ values over the globe during 2008.

94    Figure B3b shows MODIS AQUA-derived mean liquid water $R_e$ in 2008 (using MODIS Level 3

95    monthly product "Cloud Effective Radius Liquid Mean Mean").

96
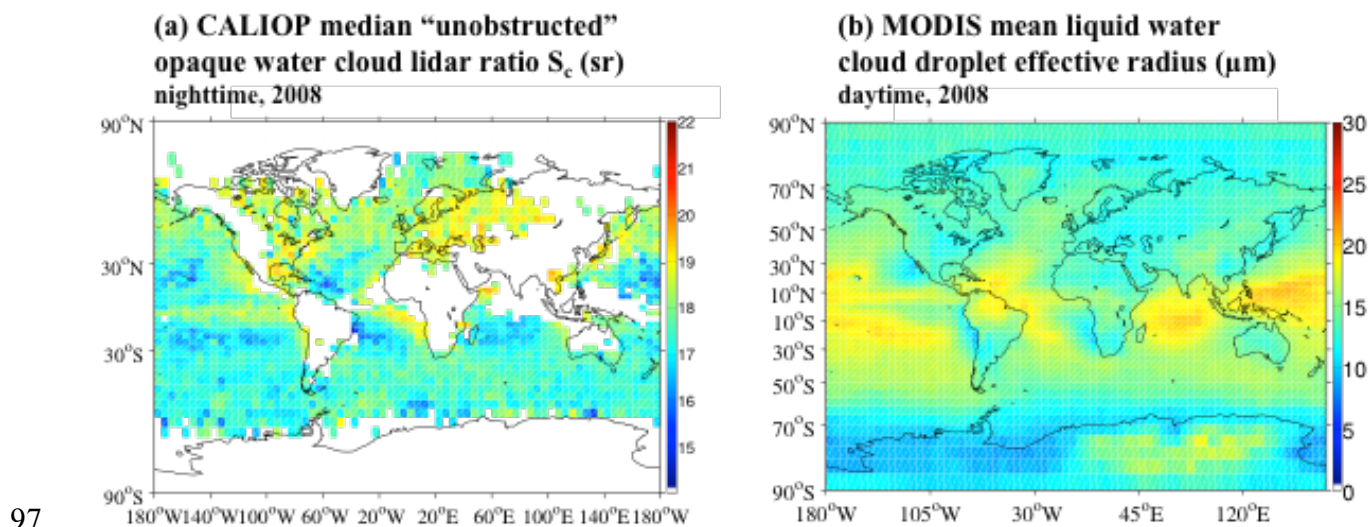
98    **Figure B3:** a) Global CALIOP yearly median nighttime "unobstructed" (i.e. clear air above) OWC lidar

99    ratio, $S_c$, in 2008 that satisfy all criteria of Table B2. For the reasons outlined in this section, any OWC

00    along the CALIOP track for which $S_c > 20$ sr or $S_c < 14$ sr is deleted before temporal and spatial

01    averaging. White pixels show a limited number of OWCs; b) Global MODIS yearly mean daytime

02    liquid water cloud droplet effective radius, $R_e$ (in μm, "Cloud Effective Radius Liquid Mean Mean"

03    parameter from MODIS MYD08_M3 product).

04

05      Greater $S_c$ values paired with lower cloud $R_e$ can be seen offshore and close to the west coasts of Africa

06      and the Americas on Figure B3. Other notable regions of low cloud $R_e$ and high $S_c$ on Figure B3 are

07      above industrial regions like northern Europe, the eastern US and South East Asia. These results appear

08      to support Twomey's analysis [Twomey, 1977; Rosenfeld and Lensky, 1998], showing an enhancement

09      of the cloud albedo through the increase of droplet number concentration and a decrease in the droplet

10      size driven by increased aerosol concentration. On the other hand, Figure B3a mostly exhibits low $S_c$

11      values (paired with large $R_e$) over the inter-tropical convergence zone (ITCZ), likely associated with

12      deep convective regimes. In addition, Figure B3a generally shows larger OWC $S_c$ values in the northern

13      hemisphere than in the southern hemisphere, which we attribute to differences in sources of cloud

14      condensation nuclei. Figure B3b shows patterns that are generally similar to those in Figure B3a, but of

15      opposite intensity. Let us note that the polarization measurements from the space-borne POLDER

16      sensor [Deschamps et al., 1994] were also used to estimate $R_e$ of liquid water clouds over the globe

17      [Bréon and Colzy, 2000] and seem to be in qualitative agreement with the findings of Figure B3b.

18      During our assessment of 5 years of CALIOP data over the globe, we have observed significantly

19      higher "unobstructed" OWC $S_c$ values (i.e., $S_c > 20$ sr, not shown on Fig B3a) near the coasts of West

20      Africa and over the region of SE Asia (e.g., see Young et al., [2018]). These may be physically

21      plausible and either (1) associated with small cloud $R_e$, resulting from the Twomey's effect as explained

22      above or (2) associated with the presence of light-absorbing aerosols residing within the OWCs

23      [Mishchenko et al., 2014; Chylek and Hallett, 1992; Wittbom et al., 2014]. These aerosols would be

24      undetected in our $IAB^{mol}_{aboveCloud}$ clear air selection method (see section B2) and would impact the

25      chemical composition of the cloud droplets, modifying their backscattered light. The latter is well

26   illustrated in Fig. 8 of Deaconu et al. [2017], which shows simulations of cloud $S_c$ with an imaginary

27   part of the refraction index equals to 0.0001, as a function of cloud droplet effective radius. Other

28   reasons for these unusually high $S_c$ values could be the sources of uncertainty noted (a), (b), (c) and (d)

29   in the beginning of section B, with (c) (i.e., the SNR of the backscatter data within the layer) possibly

30   having a much higher impact on $S_c$ than all other factors. An additional source of uncertainty on the

31   retrieval of $S_c$ could be a failure of the CALIPSO surface detection scheme. If CALIOP fails to detect

32   the surface adequately, part of the Earth's surface could be misclassified as an opaque water cloud and

33   these misclassified clouds would have abnormally high $S_c$.

34   Let us note that the vast majority of the $S_c$ values reported in the literature (i.e., in Hu et al., [2006], Liu

35   et al. [2015] and Deaconu et al., [2017]) are estimated using a Mie code and not directly measured.

36   However, none of these results show $S_c$ values above 20 sr for non-aerosol-contaminated OWCs. On the

37   other hand (and to add a lower bracket on our OWC $S_c$ calculations), none of these results show $S_c$

38   values below 14 sr. For this reason, we have imposed an additional threshold on the OWC $S_c$ values as

39   part of step (S3) in Table B1: we delete any "unobstructed" OWC along the CALIOP track for which $S_c$

40   > 20 sr (i.e., unrealistically small water cloud droplets) or an $S_c$ < 14 sr (i.e., unrealistically large water

41   cloud droplets). Every OWC $S_c$ value along the CALIOP track was then compiled to produce four

42   global median seasonal 4º×5º maps of OWC $S_c$ using 5 years of night-time CALIOP data (from 2008 to

43   2012).

44    There is additional precedent for establishing an upper limit of $S_c = 20$ sr. Note that, from Eq. B6, the

45    value of $IAB^{OWC}_{SS,CAC}$ corresponding to $S_c = 20$ sr is $0.025$ $sr^{-1}$. As mentioned earlier, this is the same

46    OWC IAB threshold value used by Chand et al. [2008] to identify their "clear air above" cases.

**Data Availability:**

This study used the following A-Train data products: (i) CALIPSO version 3 lidar level 1 profile products (Powell et al. [2013]; NASA Langley Research Center Atmospheric Science Data Center; https://doi.org/10.5067/CALIOP/CALIPSO/CAL_LID_L1-ValStage1-V3-01_L1B-003.01; last access: 26 September 2018), (ii) CALIPSO version 3 lidar level 2 5 km cloud layer products (Powell et al. [2013]; NASA Langley Research Center Atmospheric Science Data Center; https://doi.org/10.5067/CALIOP/CALIPSO/CAL_LID_L2_05kmCLay-Prov-V3-01_L2-003.01; last access: 26 September 2018), (iii) MODIS Atmosphere L2 Version 6 Aerosol Product (Levy and Hsu [2015]; NASA MODIS Adaptive Processing System, Goddard Space Flight Center, USA; http://dx.doi.org/10.5067/MODIS/MOD04_L2.006; last access: 26 September 2018), and (iv) L2 Version 3 OMI products OMAERO [Stein-Zweers and Veefkind, 2012] and OMAERUV [Torres, 2006].

**Author contributions:**

The overarching research goals were formulated by Dr Redemann. Dr. Kacenelenbogen, Dr. Young and Mr. Vaughan influenced the evolution of these research goals. Dr. Kacenelenbogen carried out the formal analyses, investigations and visualizations and wrote the original draft. All co-authors have reviewed and edited the multiple drafts of the manuscript. The methodology behind the global application of the DR method to CALIOP measurements was first developed by Dr. Hu, and adapted by Dr. Kacenelenbogen, Dr. Young, Mr. Vaughan, and Ms. Powell to accommodate the requirements of

69    this study. The methodology for using this combination of A-Train satellites to infer aerosol intensive

70    radiative properties was conceptualized by Dr Redemann. The joint MODIS-OMI-CALIOP aerosol

71    radiative properties were developed and provided by Dr. Shinozuka, Mr. Livingston and Ms. Zhang. Dr.

72    LeBlanc performed the radiative transfer calculations that provided Direct Aerosol Radiative Effects

73    estimates in clear skies and above clouds.

75    **Competing interests:**

76    The authors declare that they have no conflict of interest.

78    **Acknowledgements:**

79    We thank the CALIPSO lidar science working group and data management team for their efforts in

80    providing and discussing these data sets. We appreciate the comments of Dr. Devasthale and other

81    reviewers that have helped us to improve the paper. We are grateful for comments from Dr. Zuidema

82    and Dr. Wood on cloud microphysics over the South East Atlantic.  We also thank Dr. Pistone for her

83    help. This study was funded in part by NASA's Research Opportunities in Space and Earth Sciences

84    (ROSES) program under grant NNH12ZDA001N-CCST.

86    **References**

87    Alfaro-Contreras, R., Zhang, J., Reid, J. S., Campbell, J. R., and Holz, R. E., Evaluating the impact

88    of aerosol particles above cloud on cloud optical depth retrievals from MODIS, J. Geophys. Res.

89    Atmos., 119, 5410–5423, doi:10.1002/2013JD021270, 2014.

90    Alfaro-Contreras, R., Zhang, J., Campbell, J. R., and Reid, J. S., Investigating the frequency and

91    interannual variability in global above-cloud aerosol characteristics with CALIOP and OMI, Atmos.

92    Chem. Phys., 16, 47-69, doi:10.5194/acp-16-47-2016, 2016.

93    Anderson, G., Clough, S., Kneizys, F., Chetwynd, J., and Shettle, E., AFGL atmospheric constituent

94    profiles (0-120 km), Tech. Rep. AFGL-TR-86-0110, Air Force Geophys. Lab., Hanscom Air Force

95    Base, Bedford, Mass, 1986.

96    Anderson, T. E., Charlson, R. J., Winker, D. M., Ogren, J. A., and Holmen, K.: Mesoscale

97    Variations of Tropospheric Aerosols, J. Atmos. Sci., 60, 119–136, 2003.

98    Arola, A., et al., Influence of observed diurnal cycles of aerosol optical depth on aerosol direct

99    radiative effect, Atmos. Chem. Phys., 13.15: 7895-7901., 2013.

00    Bréon, F. M. and S. Colzy, Global distribution of cloud droplet effective radius from POLDER

01    polarization measurements, Geo. Reas. Lett., Vol. 27, N 24, P 4065-4068, 2000.

02    Buras, R., Dowling, T., and Emde, C., New secondary-scattering correction in DISORT with

03    increased efficiency for forward scattering, J. Quant. Spectrosc. Ra., 112, 2028–2034, 2011.

04    Candlish, L. M., R. L. Raddatz, G. G. Gunn, M. G. Asplin and D. G. Barber: A Validation of

CloudSat and CALIPSO's Temperature, Humidity, Cloud Detection, and Cloud Base Height over the Arctic Marine Cryosphere, Atmos. Ocean, 51, 249–264, doi:10.1080/07055900.2013.798582, 2013.

Chand, D., T. L. Anderson, R. Wood, R. J. Charlson, Y. Hu, Z. Liu, and M. Vaughan, Quantifying above-cloud aerosol using spaceborne lidar for improved understanding of cloudy-sky direct climate forcing, J. Geophys. Res., 113, D13206, doi:10.1029/007JD009433, 2008.

Chand, D., R. Wood, T. L. Anderson, S. K. Satheesh, and R. J. Charlson, Satellite-derived direct radiative effect of aerosols dependent on cloud cover, Nat. Geosci., 2, 181–184, doi:10.1038/ngeo437, 2009.

Chang, Ian, and Sundar A. Christopher, "Identifying Absorbing Aerosols Above Clouds From the Spinning Enhanced Visible and Infrared Imager Coupled With NASA A-Train Multiple Sensors." IEEE. T. Geosci. Remote. S., 54.6: 3163-3173, 2016.

Chang, Ian, and Sundar A. Christopher., "The impact of seasonalities on direct radiative effects and radiative heating rates of absorbing aerosols above clouds." Q. J. Roy. Meteor. Soc., 143.704: 1395-1405, 2017.

Chin, Mian. *Atmospheric aerosol properties and climate impacts*. Diane Publishing, 2009

Chung, C. E., V. Ramanathan, D. Kim, and I. A. Podgorny: Global anthropogenic aerosol direct forcing derived from satellite and ground-based observations. J. Geophys. Res., 110, D24207, doi:10.1029/2005JD006356, 2005.

Chylek, Petr, and John Hallett, "Enhanced absorption of solar radiation by cloud droplets containing soot particles in their surface." Q. J. Roy. Meteor. Soc., 118.503: 167-172, 1992.

Costantino, L. and Bréon, F.-M., Satellite-based estimate of aerosol direct radiative effect over the South-East Atlantic, Atmos. Chem. Phys. Discuss., 13, 23295-23324, doi:10.5194/acpd-13-23295-2013, 2013.

Cox, Charles, and Walter Munk. "Measurement of the roughness of the sea surface from photographs of the sun's glitter." Josa 44.11: 838-850, 1954.

Deaconu, L. T., F. Waquet, D. Josset, N. Ferlay, F. Peers, F. Thieuleux, F. Ducos, N. Pascal, D. Tanré, and P. Goloub, "Consistency of aerosols above clouds characterization from A-Train active and passive measurements", Atmos. Meas. Tech. Discuss., doi:10.5194/amt-2017-42, 2017.

De Graaf, M., L. G. Tilstra, P. Wang, and P. Stammes, Retrieval of the aerosol direct radiative effect over clouds from spaceborne spectrometry, J. Geophys. Res., 117, D07207, doi:10.1029/2011JD017160, 2012.

De Graaf, M., N. Bellouin, L. G. Tilstra, J. Haywood, and P. Stammes, Aerosol direct radiative effect of smoke over clouds over the southeast Atlantic Ocean from 2006 to 2009, Geophys. Res. Lett., 41, 7723–7730, doi:10.1002/2014GL061103, 2014.

Deschamps, P. Y., F. M. Breon, M. Leroy, A. Podaire, A. Bricaud, J. C. Buriez and G. Seze, The POLDER mission: Instrument characteristics and scientific objectives. IEEE T. Geosci. Remote. S., 32, 598-615, 1994.

43    Devasthale, A., and M. A. Thomas, A global survey of aerosol-liquid water cloud overlap based on

44    four years of CALIPSO–CALIOP data, Atmos. Chem. Phys., 11, 1143–1154, 2011.

45    Di Girolamo L, Liang L, Platnick S. A global view of one-dimensional solar radiative transfer

46    through oceanic water clouds. Geophys. Res. Lett.;37:L18809, 2010.

47    Emde, C., Buras-schnell, R., Kylling, A., Mayer, B., Gasteiger, J., Hamann, U., Kylling, J., Richter,

48    B., Pause, C., Dowling, T. and Bugliaro, L., The libRadtran software package for radiative transfer

49    calculations (version 2.0.1), Geosci. Model Dev., 9, 1647–1672, doi:10.5194/gmd-9-1647-2016,

50    2016.

51    Feng, N., and S. A. Christopher, Measurement-based estimates of direct radiative effects of

52    absorbing aerosols above clouds, J. Geophys. Res. Atmos., 120, 6908–6921, doi:10.1002/

53    2015JD023252, 2015.

54    Fu, Q. and Liou, K., On the correlated k-distribution method for radiative transfer in

55    nonhomogeneous atmospheres, J. Atmos. Sci., 49, 2139–2156, 1992.

56    Guzman, R., Chepfer, H., Noel, V., Vaillant de Guélis, T., Kay, J. E., Raberanto, P., Cesana, G.,

57    Vaughan, M. A., and Winker, D. M.: Direct atmosphere opacity observations from CALIPSO

58    provide new constraints on cloud-radiation interactions, J. Geophys. Res., 122, 1066–1085,

59    https://doi.org/10.1002/2016JD025946, 2017.

60    Haywood, J. M., and V. Ramaswamy, Global sensitivity studies of the direct radiative forcing due

61    to anthropogenic sulfate and black carbon aerosols, J. Geophys. Res., 103, 6043–6058,

62    doi:10.1029/97JD03426, 1998.

Holben, B. N., Eck, T. F., Slutsker, I., Tanré, D., Buis, J. P., Setzer, A., Vermote, E., Reagan, J. A., Kaufman, Y. J., Nakajima, T., Lavenu, F., Jankowiak, I., and Smirnov, A., AERONET−A federated instrument network and data archive for aerosol characterization, Remote Sens. Environ., 66, 1−16, 1998.

Hu, Y., Vaughan, M., Winker, D., Liu, Z., Noel, V., Bissonnette, L., Roy, G., McGill, M., and Trepte, C., A simple multiple scattering-depolarization relation of water clouds and its potential applications, Proceedings of 23nd International Laser Radar Conference, Nara, Japan, 24−28 July, 19−22, 2006.

Hu, Y., Vaughan, M., Liu, Z., Lin, B., Yang, P., Flittner, D., Hunt, W., Kuehn, R., Huang, J., Wu, D., Rodier, S., Powell, K., Trepte, C., and Winker, D.: The depolarization-attenuated backscatter relation: CALIPSO lidar measurements vs. theory, Optics Express, 15, 5327−5332, doi:10.1364/OE.15.005327, 2007a.

Hu, Y, M. Vaughan, Z. Liu, K. Powell, and S. Rodier, Retrieving Optical Depths and Lidar Ratios for Transparent Layers Above Opaque Water Clouds From CALIPSO Lidar Measurements, IEEE Geosci. Remote Sens. Lett., 4, 523-526, 2007b.

Hu, Y., et al., CALIPSO/CALIOP cloud phase discrimination algorithm, J. Atmos. Ocean. Tech., 26.11: 2293-2309, 2009.

Hunt, W. H., D. M. Winker, M. A. Vaughan, K. A. Powell, P. L. Lucker, and C. Weimer, CALIPSO lidar description and performance assessment, J. Atmos. Ocean. Tech., 26, 1214−1228, doi:10.1175/2009JTECHA1223.1, 2009.

Jethva, H., O. Torres, L. A. Remer, and P. K. Bhartia, A color ratio method for simultaneous retrieval of aerosol and cloud optical hickness of above-cloud absorbing aerosols from passive sensors: Application to MODIS measurements, IEEE T. Geosci. Remote. S., 51(7), 3862–3870, doi:10.1109/TGRS.2012.2230008, 2013.

Jethva, H., O. Torres, F. Waquet, D. Chand, and Y. Hu, How do A-train sensors intercompare in the retrieval of abovecloud aerosol optical depth? A case study-based assessment, Geophys. Res. Lett., 41, doi:10.1002/2013GL058405, 2014.

Kacenelenbogen, M., J. Redemann, M. A. Vaughan, A. H. Omar, P. B. Russell, S. Burton, R. R. Rogers, R. A. Ferrare, and C. A. Hostetler, An evaluation of CALIOP/CALIPSO's aerosol-above-cloud detection and retrieval capability over North America, J. Geophys. Res. Atmos., 119, 230–244, doi:10.1002/2013JD020178, 2014.

Kassianov, E., et al. "Do diurnal aerosol changes affect daily average radiative forcing?." Geophys. Res. Lett., 40.12: 3265-3269, 2013.

Kim, S.-W., E.-S. Chung, S.-C. Yoon, B.-J. Sohn, and N. Sugimoto, "Intercomparisons of cloud-top and cloud-base heights from ground-based Lidar, CloudSat and CALIPSO measurements", Int. J. Remote Sens., 32, 1179–1197, doi:10.1080/01431160903527439, 2011.

Kim, M.-H., A. H. Omar, M. A. Vaughan, D. M. Winker, C. R. Trepte, Y. Hu, Z. Liu and S.-W. Kim, 2017: "Quantifying the low bias of CALIPSO's column aerosol optical depth due to undetected aerosol layers", *J. Geophys. Res. Atmos.*, **122**, 1098–1113, doi:10.1002/2016JD025797.

King, Michael D., et al. "Spatial and temporal distribution of clouds observed by MODIS onboard

the Terra and Aqua satellites." IEEE T. Geosci. Remote. S., 51.7: 3826-3852, 2013.

Klein, S. A. and Hartmann, D. L., The seasonal cycle of low stratiform clouds, J. Climate, 6, 1587–1606, 1993.

Kovacs, T.: Comparing MODIS and AERONET aerosol optical depth at varying separation distances to assess ground-based validation strategies for spaceborne lidar, J. Geophys. Res., 111, D24203, doi:10.1029/2006JD007349, 2006.

Leahy, L. V., R. Wood, R. J. Charlson, C. A. Hostetler, R. R. Rogers, M. A. Vaughan, and D. M. Winker, On the nature and extent of optically thin marine low clouds, J. Geophys. Res., 117, D22201, doi:10.1029/2012JD017929, 2012.

Levy, R., and C. Hsu. "MODIS Atmosphere L2 Aerosol Product." *NASA MODIS Adaptive Processing System*, 2015.

Liu, D., Wang, Z., Liu, Z., Winker, D. M., and Trepte, C., A height resolved global view of dust aerosols from the first year CALIPSO lidar measurements, J. Geophys. Res., 113, D16214, doi:10.1029/2007JD009776, 2008.

Liu, Z., R. Kuehn, M. Vaughan, D. Winker, A. Omar, K. Powell, C. Trepte, Y. Hu, and C. Hostetler, The CALIPSO cloud and aerosol discrimination: Version 3, Algorithm and test results, 25th International Laser and radar conference, 2010.

Liu Z, D. Winker, A. Omar, M. Vaughan, J. Kar, C. Trepte, Y. Hu, and G. Schuster, Evaluation of CALIOP 532nm aerosol optical depth over opaque water clouds, Atmos. Chem. Phys., 15, 1265–1288, 2015.

23    Mace, G. G. and Protat, A.: Clouds over the Southern Ocean as Observed from The RV Investigator

24    during CAPRICORN. Part 1: Cloud Occurrence and Phase Partitioning, J. Appl. Meteor. Climatol.,

25    57, 1783–1803, doi:10.1175/JAMC-D-17-0194.1, 2018.

26    Matus, Alexander V., et al., The role of clouds in modulating global aerosol direct radiative effects

27    in spaceborne active observations and the Community Earth System Model." J. Climate, 28.8: 2986-

28    3003, 2015.

29    McGill, M. J., M. A. Vaughan, C. R. Trepte, W. D. Hart, D. L. Hlavka, D. M. Winker, and R.

30    Kuehn, Airborne validation of spatial properties measured by the CALIPSO lidar, J. Geophys. Res.,

31    **112**, D20201, doi:10.1029/2007JD008768, 2007.

32    Meyer, K., S. Platnick, L. Oreopoulos, and D. Lee, Estimating the direct radiative effect of

33    absorbing aerosols overlying marine boundary layer clouds in the southeast Atlantic using MODIS

34    and CALIOP, J. Geophys. Res. Atmos., 118, 4801–4815, doi:10.1002/jgrd.50449, 2013.

35    Meyer, K., S. Platnick, and Z. Zhang: Simultaneously inferring above-cloud absorbing aerosol

36    optical thickness and underlying liquid phase cloud optical and microphysical properties using

37    MODIS, J. Geophys. Res. Atmos., 120, 5524–5547, doi:10.1002/2015JD023128, 2015.

38    Min, M., and Z. Zhang, On the influence of cloud fraction diurnal cycle and sub-grid cloud optical

39    thickness variability on all-sky direct aerosol radiative forcing, J. Quant. Spectrosc. RA., 142: 25-

40    36, 2014.

41    Mishchenko, Michael I., et al., Optics of water cloud droplets mixed with black-carbon aerosols,

42    Opt. Lett., 39.9: 2607-2610, 2014.

43    Mitchell R. M., S. K. Campbell, and Y. Qin, Recent increase in aerosol loading over the Australian

44    arid zone, Atmos. Chem. Phys., 10, 1689– 1699, 2010.

45    O, K.-T., Wood, R., and Tseng, H.-H.: Deeper, precipitating PBLs associated with optically thin

46    veil clouds in the Sc-Cu transition, Geophysical Research Letters, 45, 5177–5184,

47    https://doi.org/10.1029/2018GL077084, 2018.

48    O'Connor, E. J., A. J. Illingworth, and R. J. Hogan, A technique for autocalibration of cloud lidar, J.

49    Atmos. Ocean. Tech., 21, 777– 786, doi:10.1175/1520-0426, 2004.

50    Oikawa, E., T. Nakajima, T. Inoue, and D. Winker, A study of the shortwave direct aerosol forcing

51    using ESSP/CALIPSO observation and GCM simulation, J. Geophys. Res. Atmos., 118, 3687–

52    3708, doi:10.1002/jgrd.50227, 2013.

53    Omar, A., et al., The CALIPSO automated aerosol classification and lidar ratio selection algorithm,

54    J. Atmos. Ocean. Tech., 26, 1994–2014, doi:10.1175/2009JTECHA1231.1, 2009.

55    Oreopoulos, Lazaros, Robert F. Cahalan, and Steven Platnick. "The plane-parallel albedo bias of

56    liquid clouds from MODIS observations." *Journal of Climate* 20.20: 5114-5125, 2007.

57    Peers F., F. Waquet, C. Cornet, P. Dubuisson, F. Ducos, P. Goloub, F. Szczap, D. Tanré, and F.

58    Thieuleux**,** Absorption of aerosols above clouds from POLDER/PARASOL measurements and

59    estimation of their direct radiative effect, Atmos. Chem. Phys., 15, 4179–4196, 2015.

60    Peng et al., The cloud albedo-cloud droplet effective radius relationship for clean and polluted

61    clouds from RACE and FIRE.ACE, J. Geophys. Res., VOL. 107, NO. D11,

62 10.1029/2000JD000281, 2002.

63 Penner, J. E., Soot and smoke aerosol may not warm climate. J. Geophys. Res., 108, 4657,

64 doi:10.1029/2003JD003409, 2003.

65 Peters, K., J. Quaas, and N. Bellouin, Effects of absorbing aerosols in cloudy skies: A satellite study

66 over the Atlantic Ocean. Atmos. Chem. Phys., 11, 1393–1404, doi:10.5194/acp-11-1393-2011,

67 2011.

68 Pinnick, R. G., Jennings, S. G., Chylek, P., Ham, C., and Grandy Jr., W. T., Backscatter and

69 extinction in water clouds, J. Geophys. Res., 88, 6787–6796, 1983.

70 Platnick, S., et al., MODIS Atmosphere L3 Monthly Product. NASA MODIS Adaptive Processing

71 System, Goddard Space Flight Center, USA, doi:10.5067/MODIS/MOD08_M3.006, 2015.

72 Platt, C. M. R., Lidar and radiometric observations of cirrus clouds, J. Atmos. Sci., 30.6: 1191-1204,

73 1973.

74 Powell, K., W. Hunt, and D. Winker, Simulations of CALIPSO Lidar Data, Proceedings of the 21st

75 International Laser Radar Conference (ILRC), Quebec City, Quebec (available at http://www-

76 calipso.larc.nasa.gov/resources/pdfs/ILRC_2002/ILRC2002_Powell_Simulator.pdf), 2002.

77 Powell, K. A., Development of the CALIPSO Lidar Simulator", M.S. Thesis, Department of

78 Applied Science, The College of William and Mary, 228 pp, 2005.

79 Powell, K. A., Liu, Z., and W. H. Hunt, Simulation of Random Electron Multiplication in CALIPSO

80 Lidar Photomultipliers, Proceedings of the 23rd International Laser Radar Conference (ILRC), Nara,

Japan (available at http://www-calipso.larc.nasa.gov/resources/pdfs/ILRC_2006/Powell-PhotomultiplierSimulation-2P-23.pdf), 2006.

Powell, K. A., et al., CALIPSO lidar calibration algorithms. Part I: Nighttime 532-nm parallel channel and 532-nm perpendicular channel, J. Atmos. Ocean. Tech., 26.10: 2015-2033, 2009.

Powell, K., Vaughan, M., Winker, D., Lee, K.-P.. Pitts, M., Trepte, C., Detweiler, P., Hunt, W., Lambeth, J., Lucker, P., Murray, T., Hagolle, O., Lifermann, A., Faivre, M., Garnier, A., and Pelon, J.: Cloud–Aerosol LIDAR Infrared Pathfinder Satellite Observations (CALIPSO) Data Products Catalog, Document No: PC-SCI-503, Release 3.5, available on-line at https://www-calipso.larc.nasa.gov/products/CALIPSO_DPC_Rev3x5.pdf (last access: 12 October 2018), 2013.

Quijano, A. L., I. N. Sokolik, and O. B. Toon, Radiative heating rates and direct radiative forcing by mineral dust in cloudy atmospheric conditions. J. Geophys. Res., 105, 12 207–12 219, doi:10.1029/2000JD900047, 2000.

Redemann, J., Vaughan, M. A., Zhang, Q., Shinozuka, Y., Russell, P. B., Livingston, J. M., Kacenelenbogen, M., and Remer, L. A., The comparison of MODIS-Aqua (C5) and CALIOP (V2 & V3) aerosol optical depth, Atmos. Chem. Phys., 12, 3025-3043, doi:10.5194/acp-12-3025-2012, 2012.

Redemann J., Y. Shinozuka, M. Kacenelenbogen, S. LeBlanc, M. Segal-Rozenhaimer, M. Vaughan, P. Stier, N. Schutgens, Use of A-Train aerosol observations to constrain direct aerosol radiative effects (DARE) and comparisons with AeroCom phase II DARE results, in preparation.

Remer, L. A., Y. J. Kaufman, D. Tanré, S. Mattoo, D. A. Chu, J. V. Martins, R.-R. Li, C. Ichoku, R. C. Levy, R. G. Kleidman, T. F. Eck, E. Vermote and B. N. Holben, The MODIS aerosol algorithm,

02      products and validation. J. Atmos. Sci.,62 (4),947-973, 2005.

03      Rogers, R. R., Hostetler, C. A., Hair, J. W., Ferrare, R. A., Liu, Z., Obland, M. D., Harper, D. B.,

04      Cook, A. L., Powell, K. A., Vaughan, M. A., and Winker, D. M., Assessment of the CALIPSO

05      Lidar 532 nm attenuated backscatter calibration using the NASA LaRC airborne High Spectral

06      Resolution Lidar, Atmos. Chem. Phys., 11, 1295-1311, doi:10.5194/acp-11-1295-2011, 2011.

07      Rosen, J., S. Young, J. Laby, N. Kjome, and J. Gras, Springtime aerosol layers in the free

08      troposphere over Australia: Mildura Aerosol Tropospheric Experiment (MATE 98), J. Geophys.

09      Res., 105(D14), 17833–17842, *doi:10.1029/2000JD900208,* 2000.

10      Rosenfeld, D. and Lensky, I. M., Satellite-based insights into precipitation formation processes in

11      continental and maritime convective clouds, B. Am. Meteorol. Soc., 79, 2457–2476, 1998.

12      Russell P. B. R., T. J. Swissler, and McCormick M. P., Methodology for error analysis and

13      simulation of lidar aerosol measurements, Appl. Optics., Vol. 18, Issue 22, pp. 3783-3797, 1979.

14      Santese, M., De Tomasi, F., and Perrone, M. R.: AERONET versus MODIS aerosol parameters at

15      different spatial resolutions over southeast Italy, J. Geophys. Res., 112, D10214,

16      doi:10.1029/2006JD007742, 2007.

17      Sayer, Andrew M., et al., Extending "Deep Blue" aerosol retrieval coverage to cases of absorbing

18      aerosols above clouds: Sensitivity analysis and first case studies, J. Geophys. Res. Atmos., 121.9:

19      4830-4854, 2016.

20      Schulz, M., Textor, C., Kinne, S., Balkanski, Y., Bauer, S., Berntsen, T., Berglen, T., Boucher, O.,

Dentener, F., Guibert, S., Isaksen, I. S. A., Iversen, T., Koch, D., Kirkevåg, A., Liu, X., Montanaro, V., Myhre, G., Penner, J. E., Pitari, G., Reddy, S., Seland, Ø., Stier, P., and Takemura, T., Radiative forcing by aerosols as derived from the AeroCom present-day and pre-industrial simulations, Atmos. Chem. Phys., 6, 5225-5246, doi:10.5194/acp-6-5225-2006, 2006.

Schutgens, N. A. J., Nakata, M., and Nakajima, T.: Validation and empirical correction of MODIS AOT and AE over ocean, Atmos. Meas. Tech., 6, 2455–2475, doi:10.5194/amt-6-2455-2013, 2013.

Shinozuka, Y. and Redemann, J.: Horizontal variability of aerosol optical depth observed during the ARCTAS airborne experiment, Atmos. Chem. Phys., 11, 8489–8495, doi:10.5194/acp-11-8489-2011, 2011.

Stamnes, K., Tsay, S.-C., Wiscombe, W., and Jayaweera, K., Numerically stable algorithm for discrete–ordinate–method radiative transfer in multiple scattering and emitting layered media, Appl. Opt., 27, 2502–2509, 1988.

Stein-Zweers D. and P. Veefkind, OMI/Aura Multi-wavelength Aerosol Optical Depth and Single Scattering Albedo 1-orbit L2 Swath 13x24 km V003, NASA Goddard Space Flight Center, Goddard Earth Sciences Data and Information Services Center (GES DISC), 10.5067/Aura/OMI/DATA2001 <https://doi.org/10.5067/Aura/OMI/DATA2001>, 2012.

Thorsen, T. J., Q. Fu, and J. M. Comstock, Comparison of the CALIPSO satellite and ground-based observations of cirrus clouds at the ARM TWP sites, J. Geophys. Res., **116**, D21203, doi:10.1029/2011JD015970, 2011.

Thorsen, T. J., and Fu, Q.: CALIPSO-inferred aerosol direct radiative effects: bias estimates using

ground-based Raman lidars, J. Geophys. Res. Atmos., 120, 12,209–12,220, doi:10.1002/2015JD024095, 2015.

Thorsen, T. J., R. A. Ferrare, C. A. Hostetler, M. A. Vaughan, and Q. Fu, The impact of lidar detection sensitivity on assessing aerosol direct radiative effects, Geophys. Res. Lett., **44**, 9059–9067, doi:10.1002/2017GL074521, 2017.

Torres O., OMI/Aura Near UV Aerosol Optical Depth and Single Scattering Albedo 1-orbit L2 Swath 13x24 km V003, Greenbelt, MD, USA, Goddard Earth Sciences Data and Information Services Center (GES DISC), 10.5067/Aura/OMI/DATA2004 <https://doi.org/10.5067/Aura/OMI/DATA2004>, 2006.

Torres, O., J. Hiren, and P. K. Bhartia, Retrieval of aerosol optical depth above clouds from OMI observations: Sensitivity analysis and case studies. J. Atmos. Sci., 69, 1037–1053, 2012.

Toth, T. D., J. R. Campbell, J. S. Reid, J. L. Tackett, M. A. Vaughan, J. Zhang, and J. W. Marquis, 2018: Minimum Aerosol Layer Detection Sensitivities and their Subsequent Impacts on Aerosol Optical Thickness Retrievals in CALIPSO Level 2 Data Products, *Atmos. Meas. Tech.*, **11**, 499–514, doi:10.5194/amt-11-499-2018.

Twomey, S., Influence of pollution on shortwave albedo of clouds, J. Atmos. Sci., 34(7), p1149–1152, doi:10.1175/1520-0469(1977) 034<1149:TIOPOT>2.0.CO;2, 1977.

Várnai, T. and A. Marshak, MODIS observations of enhanced clear sky reflectance near clouds, Geophys. Res. Lett., 36, L06807, doi:10.1029/2008GL037089, 2009.

Vaughan, M.,K. Powell, R.Kuehn, S. Young, D. Winker, C.Hostetler, W.Hunt, Z. Liu, M. McGill,

61    and B. Getzewich, Fully automated detection of cloud and aerosol layers in the CALIPSO lidar

62    measurements, J. Atmos. Ocean. Tech., 26, 2034–2050, oi:10.1175/2009JTECHA1228.1, 2009.

63    Vaughan, M. A., Z. Liu, M. J. McGill, Y. Hu, and M. D. Obland, On the spectral dependence of

64    backscatter from cirrus clouds: Assessing CALIOP's 1064 nm calibration assumptions using cloud

65    physics lidar measurements, J. Geophys. Res., 115, D14206, doi:10.1029/2009JD013086, 2010.

66    Waquet F., J. Riedi, L. C. Labonnote, P. Goloub, B. Cairns, J-L. Deuzé, and D. Tanré, Aerosol

67    Remote Sensing over Clouds Using A-Train Observations. J. Atmos. Sci., **66**, 2468–2480, 2009.

68    Waquet, F., F. Peers, F. Ducos, P. Goloub, S. Platnick, J. Riedi, D. Tanré, and F. Thieuleux, Global

69    analysis of aerosol properties above clouds, Geophys. Res. Lett., 40, 5809–5814,

70    doi:10.1002/2013GL057482, 2013a.

71    Waquet, F., et al., Retrieval of aerosol microphysical and optical properties above liquid clouds

72    from POLDER/PARASOL polarization measurements, Atmos. Meas. Tech., 6, 991–1016,

73    doi:10.5194/amt-6-991, 2013b.

74    Watson-Parris, D., Schutgens, N., Winker, D., Burton, S. P., Ferrare, R. A., and Stier, P.: On the

75    limits of CALIOP for constraining modelled free-tropospheric aerosol, *Geophys. Res. Lett.*, **45**,

76    9260–9266, doi:10.1029/2018GL078195, 2018.

77    Wen, G., A. Marshak, R. F. Cahalan, L. A. Remer, and R. G. Kleidman, 3-D aerosol–cloud

78    radiative interaction observed in collocated MODIS and ASTERg images of cumulus cloud fields, J.

79    Geophys. Res., 112, D13204, doi:10.1029/2006JD008267, 2007.

Wilcox, E. M., Direct and semi-direct radiative forcing of smoke aerosols over clouds, Atmos. Chem. Phys., 12, 139-149, doi:10.5194/acp-12-139-2012, 2012.

Winker, D. M., M. A. Vaughan, A. Omar, Y. Hu, K. A. Powell, Z. Liu, W. H. Hunt, and S. A. Young, Overview of the CALIPSO mission and CALIOP data processing algorithms, J. Atmos. Ocean. Tech., 26, 2310–2323, doi:10.1175/2009JTECHA1281.1, 2009.

Wittbom, C., Eriksson, A. C., Rissler, J., Carlsson, J. E., Roldin, P., Nordin, E. Z., Nilsson, P. T., Swietlicki, E., Pagels, J. H., and Svenningsson, B., Cloud droplet activity changes of soot aerosol upon smog chamber ageing, Atmos. Chem. Phys., 14, 9831-9854, doi:10.5194/acp-14-9831-2014, 2014.

Xu, Hui, et al. "On the influence of the diurnal variations of aerosol content to estimate direct aerosol radiative forcing using MODIS data." Atmos. Environ., 141: 186-196, 2016.

Yorks, J., D. Hlavka, M. Vaughan, M. McGill, W. Hart, S. Rodier, and R. Kuehn, Airborne Validation of Cirrus Cloud Properties Derived from CALIPSO Lidar Measurements: Spatial Properties, J. Geophys. Res., **116**, D19207, doi:10.1029/2011JD015942, 2011.

Young, S. A., and M. A. Vaughan, The retrieval of profiles of particulate extinction from Cloud Aerosol Lidar Infrared Pathfinder Satellite Observations (CALIPSO) data: Algorithm description, J. Atmos. Ocean. Tech., 26, 1105–1119, doi:10.1175/2008JTECHA1221.1, 2009.

Young, S. A., Vaughan, M. A., Garnier, A., Tackett, J. L., Lambeth, J. B., and Powell, K. A.: Extinction and Optical Depth Retrievals for CALIPSO's Version 4 Data Release, Atmos. Meas. Tech. Discuss., doi:10.5194/amt-2018-182, accepted for publication, 2018.

Young, S. A., Vaughan, M. A., Garnier, A., Tackett, J. L., Lambeth, J. B., and Powell, K. A.: Extinction and Optical Depth Retrievals for CALIPSO's Version-4 Data Release: Supplementary Material, doi:10.5194/TBD, 2018.

Yu, H., et al. "A review of measurement-based assessments of the aerosol direct radiative effect and forcing." *Atmospheric Chemistry and Physics* 6.3: 613-666, 2006.

Yu, H., Y. Zhang, M. Chin, Z. Liu, A. Omar, L. A. Remer, Y. Yang, T. Yuan, and J. Zhang, An integrated analysis of aerosol above clouds from A-Train multi-sensor measurements, Remote Sens. Environ., 121: 125–131, 2012.

Yu, H., and Z. Zhang, New directions: Emerging satellite observations of above-cloud aerosols and direct radiative forcing, Atmos. Environ., 72, 36–40, doi:10.1016/j.atmosenv.2013.02.017, 2013.

Zarzycki, C. M., and T. C. Bond, How much can the vertical distribution of black carbon affect its global direct radiative forcing?, Geophys. Res. Lett., 37, L20807, doi:10.1029/2010GL044555, 2010.

Zelinka, M. D., Klein, S. A., and Hartmann, D. L., Computing and Partitioning Cloud Feedbacks Using Cloud Property Histograms. Part I: Cloud Radiative Kernels. J. Climate, 833 25:3715–3735, 2012.

Zhang, J., J. S. Reid, and B. N. Holben, An analysis of potential cloud artifacts in MODIS over ocean aerosol optical thickness products, Geophys. Res. Lett., 32, L15803, doi: 10.1029/2005GL023254, 2005.

Zhang Z, Platnick S. An assessment of differences between cloud effective particle radius retrievals for marine water clouds from three MODIS spectral bands. J. Geophys. Res.,; 116:D20215, 2011.

Zhang Z, Ackerman AS, Feingold G, Platnick S, Pincus R, Xue H. Effects of cloud horizontal inhomogeneity and drizzle on remote sensing of cloud droplet effective radius: case studies based on large-eddy simulations. J. Geophys. Res.; 117:D19208, 2012.

Zhang, Z., K. Meyer, S. Platnick, L. Oreopoulos, D. Lee, and H. Yu, A novel method for estimating shortwave direct radiative effect of above-cloud aerosols using CALIOP and MODIS data, Atmos. Meas. Tech., 7(6), 1777–1789, doi:10.5194/amt-7-1777-2014, 2014.

Zhang, Z., Meyer, K., Yu, H., Platnick, S., Colarco, P., Liu, Z., Oreopoulos, L., Shortwave direct radiative effects of above-cloud aerosols over global oceans derived from 8 years of CALIOP and MODIS observations, Atmos. Chem. Phys., 16.5: 2877-2900, 2016.

Zuidema, P., Redemann, J., Haywood, J., Wood, R., Piketh, S., Hipondoka, M., and Formenti, P.: Smoke and Clouds above the Southeast 25 Atlantic Upcoming Field Campaigns Probe Absorbing Aerosol's Impact on Climate, Bulletin of the American Meteorological Society, 97, 1131–1135, https://doi.org/10.1175/BAMS-D-15-00082.1, 2016.